The Innovation

Report

Direct conversion of CO_2 to a jet fuel over CoFe alloy catalysts

Lei Zhang,[1,5,7] Yaru Dang,[1,2,7] Xiaohong Zhou,[2,4,7] Peng Gao,[1,2,*] Alexander Petrus van Bavel,[3] Hao Wang,[1] Shenggang Li,[1,2,4,*] Lei Shi,[1] Yong Yang,[1,4] Evgeny I. Vovk,[4] Yihao Gao,[1] and Yuhan Sun[1,4,6,*]

*Correspondence: gaopeng@sari.ac.cn (P.G.); lisg@sari.ac.cn (S.L.); sunyh@sari.ac.cn (Y.S.)

Received: May 3, 2021; Accepted: September 26, 2021; Published Online: September 29, 2021; https://doi.org/10.1016/j.xinn.2021.100170

Graphical abstract

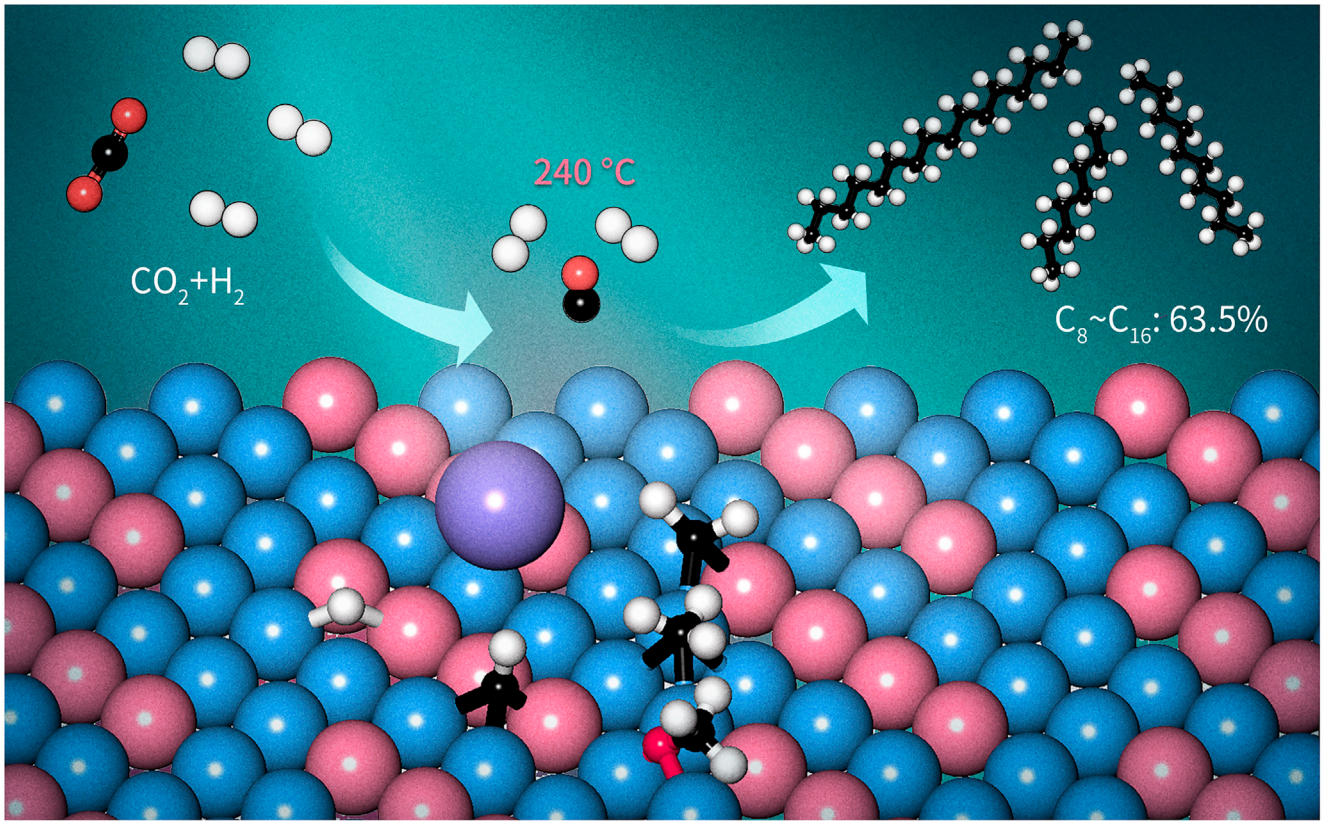

Public summary

- An alloy is developed for the direct CO_2 hydrogenation to jet-fuel-range hydrocarbons
- The selectivity of the hydrocarbons (63.5%) exceeds the theoretical maximum value
- The CoFe alloy is the active phase in the coupling reaction between surface carbons
- The CoFe alloy is a highly efficient catalyst in the presence of a sodium promoter

Direct conversion of CO_2 to a jet fuel over CoFe alloy catalysts

Lei Zhang,[1,5,7] Yaru Dang,[1,2,7] Xiaohong Zhou,[2,4,7] Peng Gao,[1,2,*] Alexander Petrus van Bavel,[3] Hao Wang,[1] Shenggang Li,[1,2,4,*] Lei Shi,[1] Yong Yang,[1,4] Evgeny I. Vovk,[4] Yihao Gao,[1] and Yuhan Sun[1,4,6,*]

[1]CAS Key Laboratory of Low-Carbon Conversion Science and Engineering, Shanghai Advanced Research Institute, Chinese Academy of Sciences, Shanghai 201210, China

[2]University of Chinese Academy of Sciences, Beijing 100049, China

[3]Shell Global Solutions International B.V., 1031HW Amsterdam, the Netherlands

[4]School of Physical Science and Technology, ShanghaiTech University, Shanghai 201210, China

[5]China-UK Low Carbon College, Shanghai Jiao Tong University, Shanghai 201306, China

[6]Shanghai Institute of Clean Technology, Shanghai 201620, China

[7]These authors contributed equally

*Correspondence: gaopeng@sari.ac.cn (P.G.); lisg@sari.ac.cn (S.L.); sunyh@sari.ac.cn (Y.S.)

Received: May 3, 2021; Accepted: September 26, 2021; Published Online: September 29, 2021; https://doi.org/10.1016/j.xinn.2021.100170

Citation: Zhang L., Dang Y., Zhou X., et al., (2021). Direct conversion of CO_2 to a jet fuel over CoFe alloy catalysts. The Innovation **2(4)**, 100170.

The direct conversion of carbon dioxide (CO_2) using green hydrogen is a sustainable approach to jet fuel production. However, achieving a high level of performance remains a formidable challenge due to the inertness of CO_2 and its low activity for subsequent C–C bond formation. In this study, we prepared a Na-modified CoFe alloy catalyst using layered double-hydroxide precursors that directly transforms CO_2 to a jet fuel composed of C_8–C_{16} jet-fuel-range hydrocarbons with very high selectivity. At a temperature of 240°C and pressure of 3 MPa, the catalyst achieves an unprecedentedly high C_8–C_{16} selectivity of 63.5% with 10.2% CO_2 conversion and a low combined selectivity of less than 22% toward undesired CO and CH_4. Spectroscopic and computational studies show that the promotion of the coupling reaction between the carbon species and inhibition of the undesired CO_2 methanation occur mainly due to the utilization of the CoFe alloy structure and addition of the Na promoter. This study provides a viable technique for the highly selective synthesis of eco-friendly and carbon-neutral jet fuel from CO_2.

Keywords: carbon dioxide hydrogenation; C–C coupling; heterogeneous catalysis; jet fuel; CoFe alloys

INTRODUCTION

The increased consumption of fossil resources is responsible for the emission of large amounts of anthropogenic CO_2, which results in climate change and ocean acidification. The recent popularization of electric cars has helped reduce gasoline consumption. Nonetheless, in the near future, liquid fuels consisting of long-chain hydrocarbons will remain a necessity for the transportation sector, especially the aviation, nautical, and land-based automotive industries.[1] Therefore, it is imperative to develop processes and technologies for the effective hydrogenation of CO_2 to liquid fuels using renewable hydrogen (H_2). Despite some breakthroughs in the synthesis of gasoline (C_5–C_{11}-range hydrocarbons) directly via CO_2 hydrogenation,[2–6] there have been few reports on the selective synthesis of jet fuel (C_8–C_{16}-range hydrocarbons).[7,8] The traditional approach to the direct synthesis of products with more than two carbons (C_{2+}) through CO_2 hydrogenation involves the carbon monoxide (CO) intermediate formed by cascading the reverse water-gas shift (RWGS) and Fischer-Tropsch synthesis (FTS) reactions. However, methanation of CO_2 or CO can also occur, which diminishes the economic value of this process.[9–11]

Of the industrially relevant FTS catalysts, Fe and Co, the Fe-based catalysts are preferred, using CO_2 as a carbon source, owing to their high RWGS activities.[9,12–14] Typically, alkenes are the main products, but large quantities of undesired CO are also formed. The alkenes are upgraded to hydrocarbon fuels over zeolites.[2,15–21] According to some recent reports, high C_{5+} selectivity (58%–65%) can be achieved using modified Fe catalysts. However, the hydrocarbon products obtained have a very broad distribution.[13,22] When following the FTS mechanism, the hydrocarbon selectivity toward a specific fraction is mainly determined by the Anderson–Schulz–Flory (ASF) distribution, which predicts that the C_8–C_{16} selectivity cannot exceed 41%.[9,23] Therefore, it is extremely challenging to achieve a higher product selectivity during jet fuel synthesis via a "one-pot" FTS process. In traditional FTS, Co-based catalysts featuring metallic Co active sites are known to have much higher chain growth capabilities and improved catalytic stability compared with Fe-based catalysts with iron carbide active sites.[24,25] However, for FTS starting from CO_2, short-chain hydrocarbons are predominantly formed, with a CH_4 selectivity of up to 70%.[12,26–29] An intuitive approach is to tune the product distribution using FeCo bimetallic catalysts. Recently, carburized CoFe catalysts have been reported to perform CO_2 hydrogenation, generating lower olefins as the main products.[18,30–33] Since, at high temperature (>280°C), CoFe catalysts can be easily carburized by CO/syngas pre-treatment or under high CO partial pressure, as in syngas conversion or the RWGS reaction,[18,30,34–36] there are few studies of C–C coupling reactions on the CoFe bimetallic alloy phase.[35–37] Therefore, it is necessary to obtain CoFe bimetallic alloy catalysts with superior performance in the selective production of jet fuel via direct CO_2 hydrogenation.

Herein, we report a Na-modified CoFe alloy catalyst for the direct hydrogenation of CO_2 to jet-fuel-range hydrocarbons. This catalyst exhibits an outstanding selectivity toward C_8–C_{16} hydrocarbons (up to 63.5%), which exceeds the maximum value predicted by the ASF model by a significant margin. In addition, it has a low combined selectivity of ~22% toward CO and CH_4. We also demonstrate that the CoFe bimetallic alloy phase is responsible for the chain propagation reaction and ensures a very high product selectivity.

RESULTS AND DISCUSSION

Composition and catalytic performance

As can be seen from Table S1, the Co/Fe atomic ratio is approximately 1.9 for the CoFe catalysts obtained by the calcination of CoFe-layered double hydroxides (LDHs), denoted as CoFe-*x*Na, where *x* represents the Na concentration in wt % (*x* = 0.23, 0.81, 3.54), and the catalyst without Na is labeled as CoFe. For comparison, catalysts without Fe (Co and Co-0.63Na with 0.63 wt % Na and 70.5 wt % Co) or Co (Fe and Fe-0.67Na with 0.67 wt % Na and 69.7 wt % Fe) were also prepared.

We assessed the CO_2 hydrogenation performance of the various catalysts, and the results are listed in Table 1. CoFe exhibits high catalytic activity, with a conversion of 19.6%, and high CH_4 selectivity of 77.3%. With increasing Na concentration, the extent of CO_2 conversion decreases gradually, with a concomitant increase in CO selectivity. The CH_4 selectivity drops significantly, while the C_{8+} selectivity increases remarkably, reaching a maximum of 64.2%

Table 1. Catalytic hydrogenation of CO_2 over various catalysts

Entry	Catalyst	Conv. (%)	CO sel. (%)	Hydrocarbon distribution (C mol %)			
				CH_4	C_2–C_4	C_5–C_7	C_{8+}
1	CoFe-3.54Na	7.0	8.8	12.7	14.9	9.2	63.1
2	CoFe-0.81Na	10.2	5.2	17.8	9.4	8.7	64.2
3	CoFe-0.23Na	12.6	5.0	55.1	5.4	0.5	39.0
4	CoFe	19.6	2.9	70.3	2.3	0.3	27.1
5	Co-0.63Na	8.3	7.2	76.5	3.6	2.3	17.5
6	Co	49.3	0.3	89.9	6.3	1.4	2.4

Standard reaction conditions: $H_2/CO_2/N_2$ ratio 73/24/3, temperature (T) 240°C, gas hourly space velocity (GHSV) 5,500 $mL \cdot g^{-1} \cdot h^{-1}$, pressure (P) 3 MPa. The data were collected after 48 h on stream.

at a Na concentration of 0.81 wt %. Compared with CoFe, CoFe-0.81Na achieves a 2.4-fold increase in C_{8+} selectivity, with a 4-fold lower CH_4 selectivity, suggesting that the effect of Na in decreasing CH_4 production is more pronounced than that in promoting C_{8+} formation. In addition, according to Figure 1A, with increasing space velocity of the feed gas, the C_{8+} fraction corresponding to CoFe-0.81Na increases substantially from 52.5% to 73.1%, along with a notable reduction in the CH_4 selectivity and CO_2 conversion, and CO formation is promoted. This indicates the suppression of CO_2 methanation at a lower conversion level. Moreover, with decreasing reaction temperature, the CH_4 selectivity declines remarkably from 26.5% to 5.8%, while the C_{8+} selectivity increases significantly from 42.2% to 81.7%, with a slight increase in CO selectivity. The catalytic activity is also decreased significantly (Figure 1B). Notably, most of the CoFe, Fe, or oxide/zeolite bifunctional catalysts developed for the hydrogenation of CO_2 to higher hydrocarbons tend to produce large amounts of the by-product, CO, partly because the RWGS reaction is favored at high reaction temperatures (>300°C).[9,38] The CO selectivity of the CoFe catalysts in previous reports exceeded 30% even at lower reaction temperatures.[18] In this study, the CO selectivity is well below 10% for all the CoFe-*x*Na catalysts at 240°C. Most of the CO_2 input is transformed to hydrocarbons on the CoFe-0.81Na catalyst. However, the CO selectivity is as high as 59.2% over Fe-0.67Na, indicating that the RWGS reaction is more likely to occur at the Fe sites modified by Na.

In additional to the low selectivity toward the undesired CH_4 and CO, the formation of light hydrocarbons (C_2–C_4) is also suppressed. A C_{5+} selectivity of up to 71.7% is observed, with the dominant products being liquid paraffins and hydrocarbon products in accordance with a double ASF model (Figure S1A).[39,40] The chain growth probability is 0.76 for C_2–C_7 (α_1) and 0.6 for heavier C_{8+} hydrocarbons (α_2). The catalyst exhibits a selectivity of 63.5% for C_8–C_{16} hydrocarbons (Figure 1C), outperforming the Fe-Mn-K catalyst reported previously for the synthesis of C_8–C_{16} hydrocarbons (47.8% of all hydrocarbons) from CO_2[7] and exceeding the maximum fraction (41%) obtained via the ASF mechanism. This differs significantly from the catalytic performance of Fe-based[13,22,41,42] or CoFe catalysts[30,34,43] with carbides as the active sites for the hydrogenation of CO_2 to higher hydrocarbons, producing olefins as the main products with very broad distributions (the highest carbon number typically exceeds 20) at higher temperatures (~300°C). In addition, we tested the performance of CoFe-0.81Na for CO hydrogenation, which afforded liquid fuels with a narrow hydrocarbon distribution (Figure S1B).

The product selectivity of the Na-modified Co catalysts changes significantly upon alloying with Fe. Comparing CoFe-0.81Na with Co-0.63Na, an increase in CO_2 conversion from 8.3% to 10.2% was observed. A more significant difference was found in the hydrocarbon distribution. For Co-0.63Na, the CH_4 selectivity is remarkably high (76.5%), while the C_{8+} selectivity is only 17.5%. The C_{8+} selectivity over CoFe-0.81Na is 64.2%, which is approximately 4-fold that of Co-0.63Na. The catalytic activity is significantly enhanced upon introducing Co. The CO_2 conversion over CoFe-0.81Na is more than twice that over Fe-0.67Na, which has a similar Na content (Table S3). Although the CH_4 selectivity over Fe-0.67Na is as low as 17.2%, the C_{8+} selectivity of 44.1% is considerably lower than that over CoFe-0.81Na. A similar trend was observed for catalysts without Na. Compared with the pure Co catalyst, the CoFe catalyst exhibits significantly higher C_{8+} selectivity and lower CH_4 selectivity. A C_{8+} selectivity of 6.8% is achieved over the pure Fe catalyst, with a reduced CH_4 selectivity of 50.9% (Table S3), while the CO_2 conversion (9.1%) is much lower than that over the Co (49.3%) or CoFe (19.6%) catalysts. The stability of the CoFe-0.81Na catalyst was also investigated. The catalyst required less than 48 h to reach a steady-state operation (Figure 1D). However, the C_8–C_{16} selectivity increased and a similar amount of time was required for the process to stabilize on stream. The CO selectivity increased continuously and stabilized at 8.5% after approximately 110–120 h. In the stability test, the extent of CO_2 conversion decreased from 14.8% to 10.6% during the initial 28 h and was maintained at 10.5% after 120 h. Similar trends were observed for CoFe-3.54Na with respect to time when the process was conducted on stream (Figure S2A). For the CoFe catalyst without Na and catalysts without Fe, the incubation time was shortened to 8 h (Figures S2B–S2D).

Structural characterization

Uncalcined CoFe-LDH precursors have lamellar structures (Figures 2A, S3, and S4). X-ray diffraction (XRD) analysis showed that the typical (001) basal reflection peaks of LDH materials were absent from the calcined samples (Figures S5A and 2C). A new phase of Fe^{III}-substituted Co_3O_4 ($Co^{II}Co^{III}Fe^{III}O_4$), hereafter denoted as Co_2FeO_4, was detected for the CoFe-*x*Na catalysts. The LDH-derived catalysts maintain the layered structure (Figures S3 and S6A), which promotes metal dispersion.[44] In addition, compared with other samples, CoFe-0.23Na and CoFe-0.81Na exhibited much higher specific surface areas (Table S1). Further reduction of CoFe-*x*Na in a pure H_2 atmosphere at 400°C for 6 h yielded cubic Co_7Fe_3 alloy nanoparticles, and no other phases were detected (Figures S5B and S6D). The CoFe alloy nanoparticle sizes of CoFe-0.81Na increased after reduction (Figures S6B and S6C). The influence of Na ions on the formation of the CoFe alloy phase was investigated using *in situ* XRD and H_2 temperature-programmed reduction (TPR) measurements, the results of which are illustrated in Figures S7 and S8, respectively. Initially, Co_2FeO_4 was reduced to CoO and FeO as the reduction temperature increased from 200°C to 350°C, and this process had negligible effect on the Na content. The Co_7Fe_3 alloy phase was formed when the reduction temperature exceeded 400°C. The introduction of excess Na inhibited the reduction of CoO and FeO to metallic Co and Fe, respectively. The addition of Na also suppressed the reduction of CoO to Co over Co-0.63Na.

On examination of the XRD patterns of the spent catalysts (Figures S5C and S5D), highly crystallized Co and poorly crystallized CoO phases were detected for Co and Co-0.63Na after 48 h of reaction. The occurrence of solely the Co_7Fe_3 alloy phase for the spent CoFe-*x*Na catalysts indicated that the formation of the CoFe alloy structure inhibited the oxidation of metallic Co during CO_2 hydrogenation. We also performed transmission electron microscopy (TEM) and scanning TEM (STEM)-energy dispersive X-ray spectrometry (EDX) characterizations to investigate the morphology and elemental distribution of the reduced and spent CoFe-*x*Na catalysts. No phase segregation was observed, and only the Co_7Fe_3 alloy phase was found after the CO_2 hydrogenation reaction (Figures 2A, 2B, S9, and S10). In addition, the oxygen was primarily distributed in the outer shell region of the spent CoFe alloy nanoparticles, whereas Na was homogeneously distributed in the CoFe alloy particles of the reduced and spent catalysts (Figures 2B and S10).

To determine the fine structure of CoFe-0.81Na, we performed X-ray adsorption near-edge structure (XANES) and extended X-ray adsorption fine structure (EXAFS) experiments (Figures 2E, 2F, and S11). The Co and Fe K-edge XANES spectra of the reduced and spent CoFe-0.81Na catalysts were similar, and the peaks at 7,111 and 7,712 eV corresponded to the 1s to 3d transitions in Fe^0 and Co^0, respectively, indicating that the Co and Fe species were mainly present in the metallic form. The Co-O and Fe-O

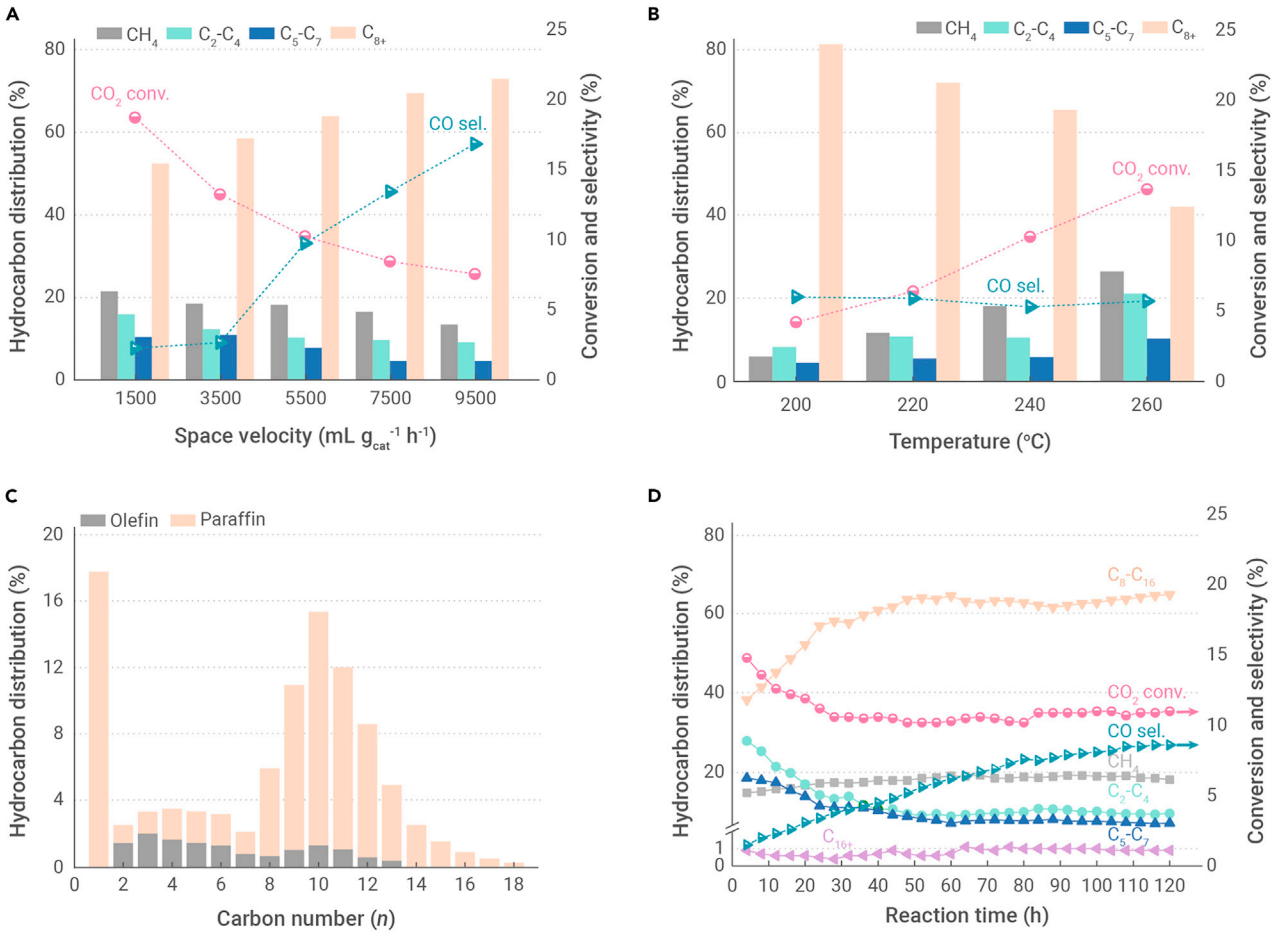

Figure 1. The evaluation data of CO_2 hydrogenation (A and B) Effects of (A) space velocity and (B) reaction temperature on conversion of CO_2, selectivity of CO, and hydrocarbon distribution. (C) Detailed distribution of hydrocarbons without CO obtained over CoFe-0.81Na under reaction conditions shown in Table 1. (D) Catalytic stability of CO_2 hydrogenation over the CoFe-0.81Na catalyst under standard reaction conditions.

coordination shells were absent from both the reduced and the spent samples, while new Co-Fe (Fe-Co) coordination shells were observed in both (Figures 2E and 2F), which indicates that the CoFe alloy structure is formed after the reduction and remains stable during the reaction. Fitting of the Co and Fe edge EXAFS data also reveals the formation of new Co-Fe bonds after the reduction (Tables S4 and S5). In addition, the Co-Fe (Co) and Fe-Co (Fe) coordination numbers increase slightly after the reaction.

To investigate the CO_2 adsorption properties of the Co, Co-0.63Na, and CoFe-*x*Na catalysts, their surface basicity was measured using CO_2 temperature-programmed desorption (TPD). With increasing Na content, the CO_2 desorption peaks were shifted to higher temperatures and the total number of basic sites increased significantly (Figure 2D). Compared with Co and Co-0.63Na, the peaks associated with weakly (50°C–200°C) and strongly (>200°C) basic sites were observed at much higher temperatures for the CoFe and CoFe-0.81Na samples, indicating that the formation of the Co_7Fe_3 alloy structure strengthened the chemisorption of CO_2. As can be seen from the H_2-TPD profiles (Figure S12A), the desorption peaks at 150°C–400°C, which are related to the hydrogenation ability of the samples and spillover or subsurface hydrogen adsorption,[42,45] were shifted to higher temperatures with increasing Na content, indicating that the hydrogenation ability is weakened upon addition of Na. H_2 desorption from CoFe and CoFe-0.81Na occurs at higher temperatures than from the corresponding samples without Fe, which indicates the lower reactivity of the hydrogen species adsorbed on the CoFe and CoFe-0.81Na surfaces. The enhanced CO_2 adsorption and weakened hydrogenation ability inhibit CH_4 production and increase the chain growth probability owing to the lower ratio of hydrogen to carbon species on the sample surface.[14,46] As shown in Figure S12B, CO adsorption on CoFe in the high-temperature desorption regions (200°C–400°C) is remarkably enhanced compared with that on Co, particularly in the presence of Na, which favors the transformation of the CO intermediates in the tandem process.[19] However, the degree of transformation decreases with increasing Na concentration. Therefore, the Co_7Fe_3 alloy structure inhibits CH_4 formation and plays a crucial role in the selective hydrogenation of CO_2 to the higher hydrocarbons that constitute jet fuel.

In situ DRIFTS study

The CO_2 activation and hydrogenation reactions over the Co and CoFe catalysts were studied using *in situ* diffuse reflectance infrared Fourier transform spectroscopy (DRIFTS). As shown in Figure S13, compared with the CO_2-DRIFTS results of CoFe, the infrared (IR) peak intensities corresponding to the surface carbonate, bicarbonate, and formate species, which are important intermediates formed during the RWGS reaction,[42] for the Co catalyst are markedly weakened, which is consistent with the results of the CO_2-TPD analysis. This leads to a lower activity of the Co catalyst toward RWGS.

Switching from CO_2 to pure H_2 over the CoFe catalyst at 240°C led to the immediate formation of gaseous CO (2,178 and 2,117 cm^{-1}), the concentration of which decreased sharply after a few minutes (Figure S14). As shown in Figures 3A and S14, along with the consumption of CO, CH_4, and C_{2+}, paraffins and olefins were detected after only 3 min. The band intensities of the higher olefins were very weak, while those of the higher paraffins increased remarkably during the initial 30 min and stabilized in the following 60 min,

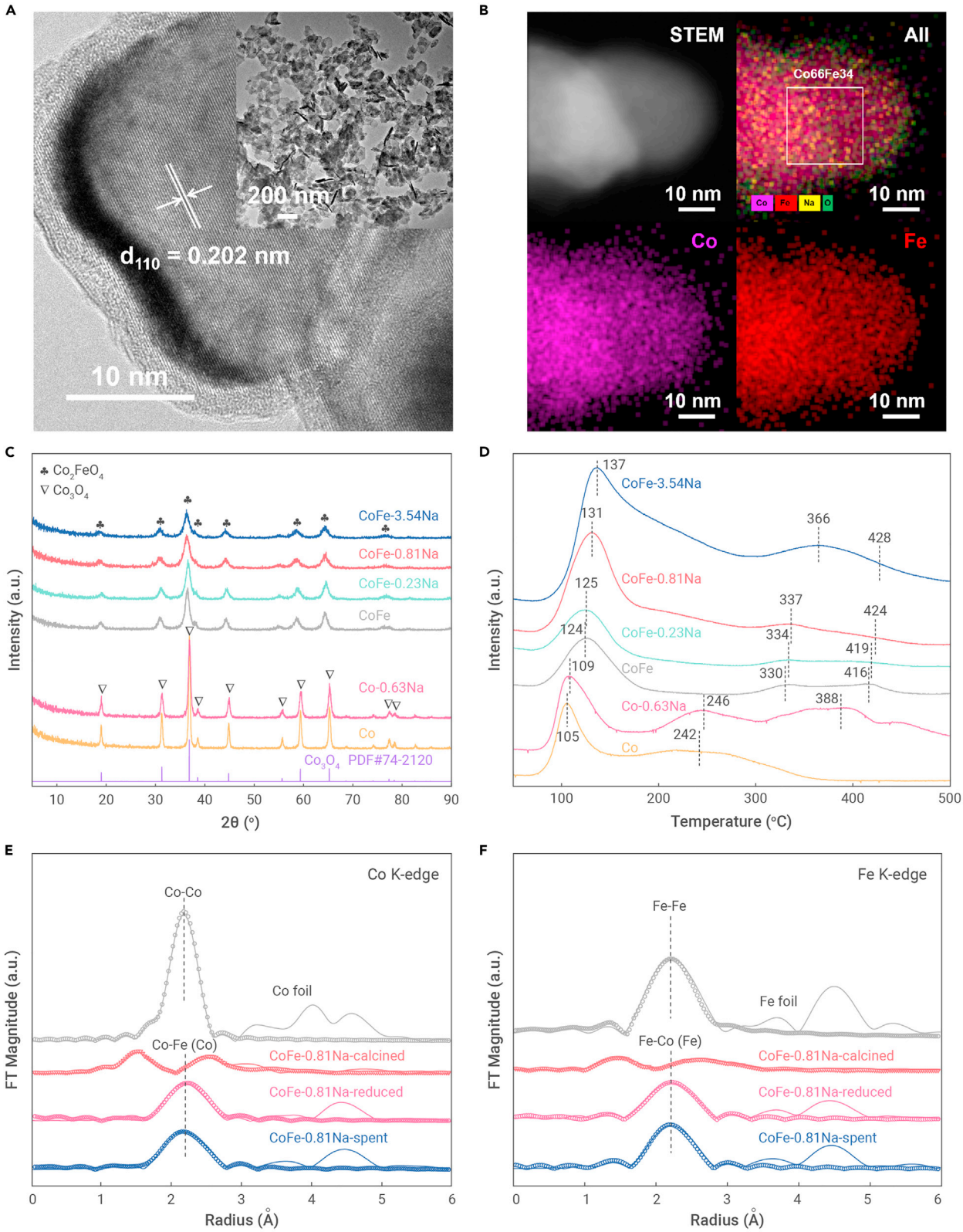

Figure 2. Catalyst characterization (A) High-resolution TEM image of spent CoFe-0.81Na and TEM image (inset) of the corresponding uncalcined precursors. (B) STEM image with the corresponding elemental mapping of spent CoFe-0.81Na. (C) XRD patterns of the samples after calcination. (D) CO_2-TPD profiles of various calcined samples. (E and F) Fourier transforms of the k^3-weighted EXAFS spectra (solid lines) and fitted curves (circles) of the calcined, reduced, and spent CoFe-0.81Na (after reaction for 48 h) and reference samples at the (E) Co K-edge and (F) Fe K-edge.

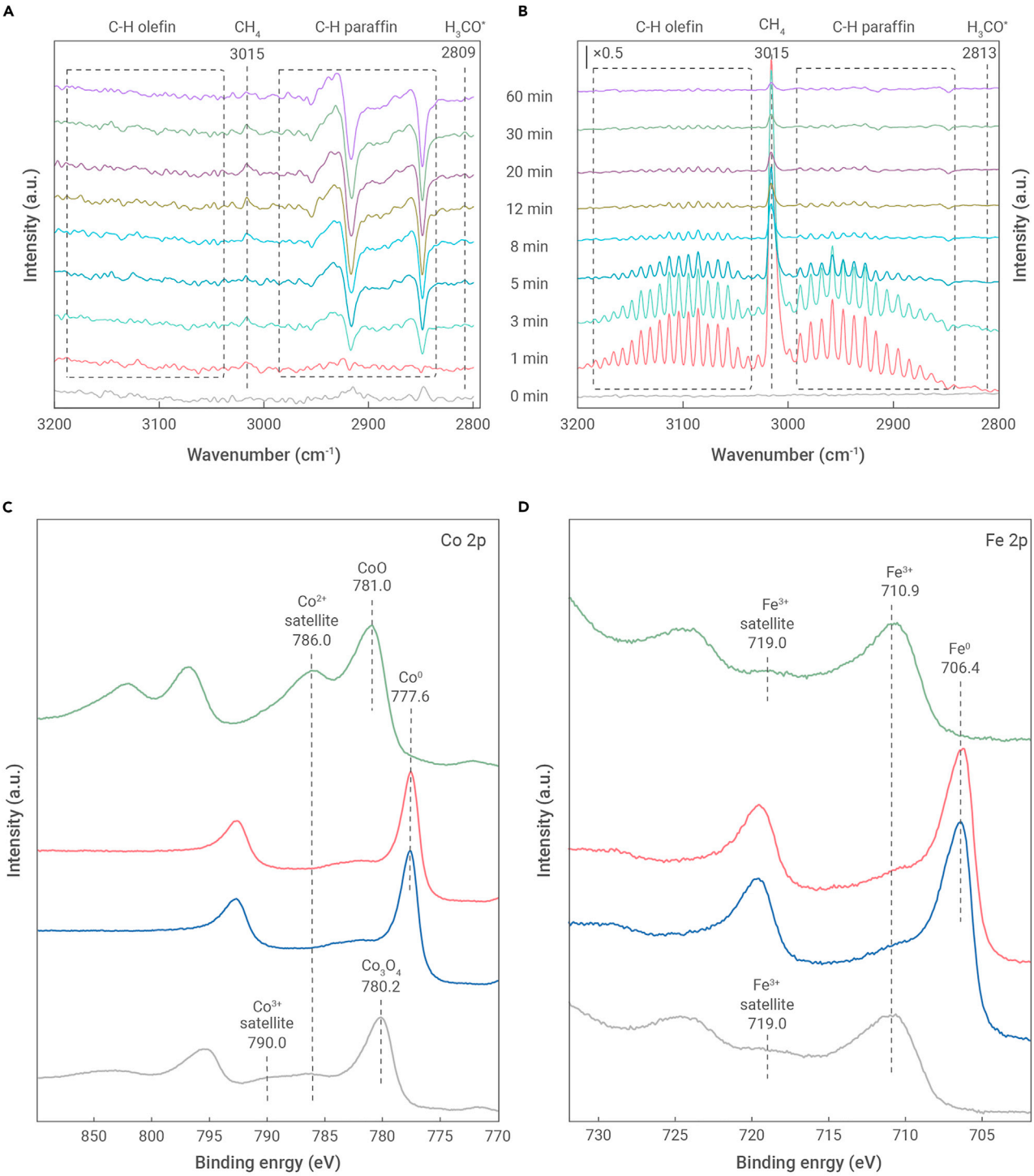

Figure 3. ***In situ*** **characterization** (A and B) DRIFTS spectra were recorded for CO_2 hydrocarbon reaction over (A) CoFe and (B) Co at 240°C. (C and D) XPS (C) Co 2p and (D) Fe 2p core level spectra of fresh CoFe-0.81Na catalyst (gray curves), after reduction in pure hydrogen (blue curves), and after CO_2 hydrogenation reaction at 200°C (red curves) or 240°C (green curves).

indicating that the C_{2+} paraffins were the principal hydrocarbons formed over CoFe. After 8 min of H_2 flow, methoxy species (CH_3O*, 1,036 and 2,809 cm^{-1}) were also detected, and the intensity of the band corresponding to CH_4 increased. Compared with the IR bands over CoFe, the band intensity of the methoxy species was enhanced and that of CH_4 was significantly lowered over CoFe-0.81Na. For the pure Co catalyst, the bands corresponding to CH_4 and the higher hydrocarbons were observed after only 1 min of H_2 flow (Figure 3B), and the band intensity of CH_4 was much stronger than those of the higher hydrocarbons, indicating that the methanation activity of the Co catalyst was considerably higher. The intensities of these bands over Co decreased significantly upon exposure to H_2 flow. In addition, the band assigned to the methoxy species disappeared after 3 min. These results indicate that the formation of CH_4 may be related to the methoxy species. Compared with the pure Co catalyst, the band intensities for CH_4 are much weaker over CoFe, suggesting that the CoFe catalyst has a lower activity toward CO_2 methanation.

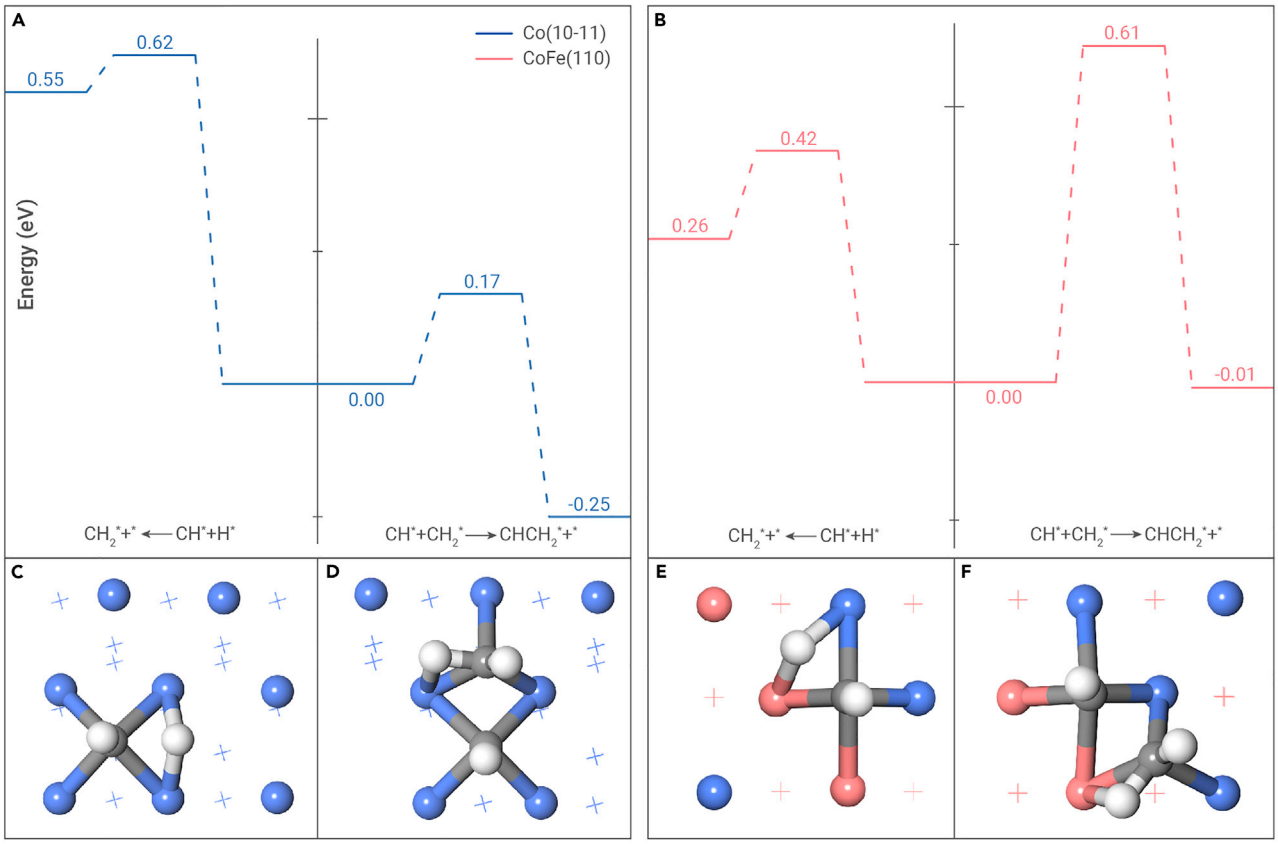

Figure 4. DFT prediction of the relative reactivities of hydrogenation and C–C coupling reactions (A and B) Potential energy profiles for CH* hydrogenation versus CH* + CH_2* coupling on the Co and CoFe alloy phases modeled by the (A) Co(10-11) and (B) CoFe(110) slabs. (C–F) Structures of the optimized transition states for (C and E) CH* hydrogenation and (D and F) CH* + CH_2* coupling on the (C and D) Co(10-11) and (E and F) CoFe(110) slabs, respectively (colors of surface atoms: Co, blue; Fe, magenta; C, gray; H, white).

Active sites

The XRD, STEM-EDX, and XAFS results confirm that the CoFe alloy species are the active phases participating in CO_2-based FTS. However, Co^{2+} and Fe^{3+} species were detected on the spent CoFe-*x*Na surface through *ex situ* X-ray photoelectron spectroscopy (XPS) analysis (Figure S15). To reveal the sites responsible for CO_2 activation and the formation of hydrocarbon products, we investigated the evolution of the surface electronic structure of CoFe-0.81Na during the CO_2 activation/hydrogenation process using XPS in an ultra-high-vacuum chamber directly connected to the high-pressure reaction cell. The Co 2p spectrum of the as-prepared sample has a profile similar to that of Co_3O_4, with a peak at 780.2 eV for Co $2p_{3/2}$ and two shoulder peaks at 787 and 790 eV (Figure 3C).[47] The Fe 2p spectrum of the as-prepared sample is consistent with that of Fe_2O_3 reported elsewhere (Figure 3D).[48] After reduction, both the Co $2p_{3/2}$ and the Fe $2p_{3/2}$ peaks became much sharper and were shifted toward the lower binding energies of 777.6 and 706.4 eV, confirming their nearly complete reduction (Figures 3C, 3D, and S16), and demonstrating the presence of the CoFe alloy.

After the subsequent reaction at 200°C for 5 h, no noticeable changes were observed in the Co 2p and Fe 2p spectra, which confirms the metallic states of the elements under the above reaction conditions. However, significant changes were observed in the spectra when CO_2 hydrogenation was performed at 240°C over the reduced sample. The Co 2p spectrum exhibits a Co $2p_{3/2}$ peak at 781 eV and a prominent Co^{2+} satellite peak, indicating the transformation of the surface metallic Co to CoO (Figure 3C). The Fe 2p spectrum after reaction at 240°C is similar to that of the fresh catalyst containing Fe^{3+} species (Figure 3D). These results are consistent with the STEM-EDX results of the spent CoFe-based catalysts (Figures 2B and S10). The oxidation of the metal is attributed to its exposure to oxidative products, such as water, at higher concentrations and temperatures. Previous studies suggest that the formation of iron oxide on the CoFe alloy surface due to oxidation promotes the formation of surface CO intermediates via RWGS,[49] which facilitates the formation of long carbon chains during the subsequent FTS process. Thus, the C_{8+} selectivity over the CoFe catalysts is much higher than that over Co catalysts. Moreover, it can be seen from Figures 3C, 3D, S15, and S16 that no iron or cobalt carbides were observed when the reaction was performed at 240°C.

Reaction mechanism

To elucidate the influence of the catalyst structure on the selectivity toward long-chain hydrocarbons, density functional theory (DFT) calculations were performed to predict the energetics of hydrogenation and self- and cross-coupling of the CH_x (x = 1, 2) species formed via CO activation (Table S6), which have been suggested to influence the chain growth probability during the FTS reactions.[35,50,51] Although CoO species may exist on the CoFe catalyst surface, chain growth typically occurs over metallic Co surfaces. We postulate that as long as the intermediate species has a CH or CH_2 moiety, it can couple with another unsaturated hydrocarbon species such as CH or CH_2, leading to continued carbon chain growth until the CH or CH_2 moiety is hydrogenated, which results in chain termination. Therefore, we first compared the differences in the energy barriers for the hydrogenation of the CH adsorbate (denoted as CH*) and its coupling with the CH_2 adsorbate (denoted as CH_2*) on the Co(10-11) and CoFe(110) slab models. As shown in Figure 4A, over the Co(10-11) surface, CH* + CH_2* coupling involves a much lower energy barrier (0.17 eV) than CH* hydrogenation (0.62 eV). The

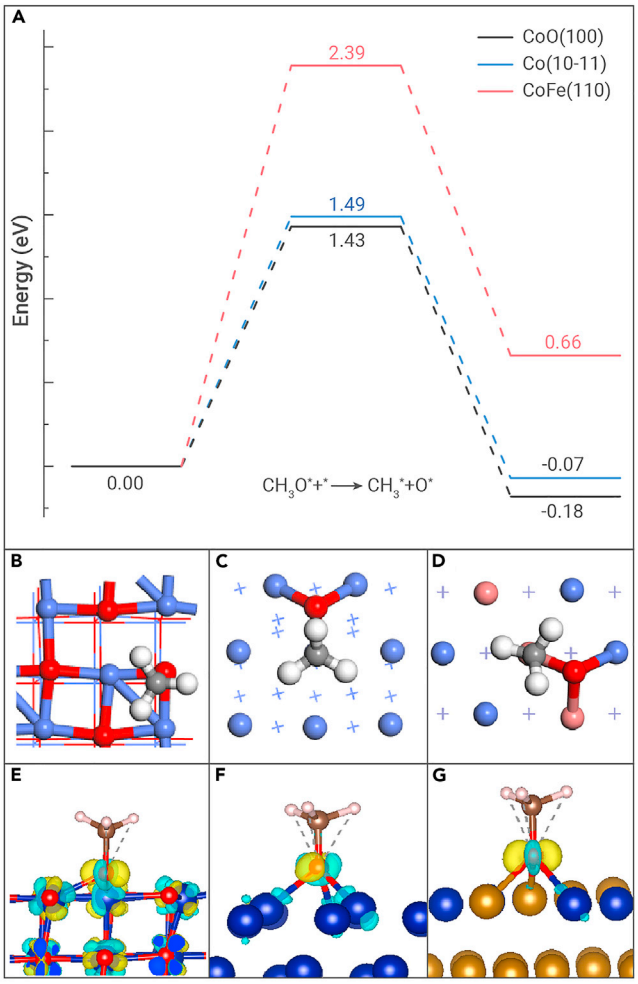

Figure 5. DFT calculations on the rate-determining step of the CO_2 methanation reaction (A) Potential energy profiles for CH_3O dissociation on the CoO, Co, and CoFe alloy phases modeled by the CoO(100), Co(10-11), and CoFe(110) slab models. (B–D) Structures of the transition states on (B) CoO(100), (C) Co(10-11), and (D) CoFe(110) (additional surface atomic color: O, red). (E–G) Charge density difference plots upon CH_3O adsorption on (E) CoO(100), (F) Co(10-11), and (G) CoFe(110), where the light blue and light yellow regions represent charge depletion and charge accumulation.

coupling reaction on the CoFe(110) surface also involves a relatively low energy barrier and is thermodynamically more favorable than hydrogenation, as shown in Figure 4B, although the energy barrier of CH* hydrogenation (0.42 eV) is somewhat lower than that of CH* + CH_2* coupling (0.61 eV). These results suggest that the Co catalyst favors chain growth over chain termination, which is important for the generation of long-chain hydrocarbons. However, Co has negligible activity toward RWGS, which restricts the formation of long-chain hydrocarbons during CO_2 hydrogenation owing to the scarcity of CH*/CH_2* species on the Co surface. In contrast, the CoFe alloy catalyst is less efficient at promoting chain growth. The transition states for CH* hydrogenation and CH* + CH_2* coupling reactions are shown in Figures 4C–4F. As shown in Figure S17A, CH_2* self-coupling on the Co(10-11) surface involves a much lower energy barrier (0.38 eV) compared with that on the CoFe(110) surface (0.51 eV), and it is also lower than that of CH_2* hydrogenation on the Co(10-11) surface (0.53 eV). These computational results suggest that the CoFe alloy phase is less favorable for the carbon chain propagation than the Co phase. Structures of the transition states involved in CH_2* hydrogenation and self-coupling on the above two surfaces are shown in Figures S17B–S17E, whereas those of the initial and final states are presented in Figures S18 and S19. The active site identified by these studies is consistent with that obtained via charge density analysis, as shown in Figure S20.

Considering that the Na promoter significantly affects both the activity and the selectivity of the Co and CoFe alloy catalysts, we further calculated the energy barriers to hydrogenation and self- and cross-coupling of CH_x over the Na-promoted Co(10-11) and CoFe(110) catalyst models. As illustrated in Figure S21 (with the additional data listed in Table S6 in parentheses), the computational results, which indicate that the addition of the Na promoter to the Co catalyst leads to a lower catalytic activity, are consistent with the experimentally observed reduced CO_2 reactivity and increased CO selectivity over the Co catalyst upon Na addition. However, for the CoFe alloy catalyst, the Na promoter favors the coupling over hydrogenation, as evidenced by the significantly higher C_{8+} selectivity and lower CH_4 selectivity.

It can be concluded from the above theoretical analysis that Co is a stronger promoter of chain growth, with a significantly higher energy barrier to CH* hydrogenation, while the main product formed during CO_2 hydrogenation over both the Co and the Co-0.63Na catalysts is CH_4. Therefore, we suggest two pathways for CO_2 hydrogenation, namely CO_2 methanation and RWGS + FTS, with the latter pathway facilitating the formation of both CH_4 and long-chain hydrocarbons. For an improved understanding of the significantly lower CH_4 selectivity over the CoFe and CoFe-0.81Na catalysts compared with the corresponding Co-based catalysts, we performed additional DFT calculations to study the methanation activity. Previous studies suggest that the dissociation of the CH_3O* species into CH_3* + O* is rate limiting during CO_2 methanation.[52] For the catalysts used in this study, three possible phases can be relevant, namely the Co, CoFe, and CoO phases. Moreover, the CoFe alloy was found to suppress CH_4 formation via CO_2 methanation. The structures of the Co(10-11), CoFe(110), and CoO(100) slab models and the corresponding structures of the CH_3O* adsorbates on these surfaces are presented in Figures S22 and S23, respectively. As can be seen in Figure 5A, the energy barrier to CH_3O* dissociation on the CoO(100) surface with a surface O vacancy is the lowest at 1.43 eV, whereas it is slightly higher at 1.49 eV on the Co(10-11) surface, and much higher at 2.39 eV on the CoFe(110) surface. The corresponding transition states are shown in Figures 5B–5D. Therefore, according to our calculations, both the Co and the CoO phases are more favorable for CO_2 methanation than the CoFe phase, which is in agreement with our experimental findings. Moreover, the gradual increase in CO_2 methanation activity over CoFe-0.81Na with increasing reaction temperatures may also be attributed to the CoO phase formed *in situ* during the reaction. Notably, the reaction energies corresponding to CH_3O* dissociation also follow the same trend, which is consistent with the correlation between the energy barriers and the corresponding reaction energies in accordance with the Brønsted-Evans-Polanyi (BEP) relationship.[53] Furthermore, as shown in Figures 5E–5G, the differences in reactivity of the above three surfaces toward CH_3O* dissociation were rationalized by performing charge density difference ($\Delta\rho$) analyses. Therefore, our DFT calculations and theoretical analyses suggest that the CoFe alloy surface has a remarkable inhibitory effect on CH_4 production via CO_2 methanation.

Conclusions

Herein, we report on a Na-modified CoFe alloy catalyst that enables the efficient production of jet-fuel-range hydrocarbons via direct CO_2 hydrogenation. The selectivity toward C_8–C_{16} hydrocarbons is as high as 63.5% at 10.2% CO_2 conversion. The catalyst demonstrates a high carbon efficiency, with a combined selectivity of approximately 22% toward undesired CH_4 and CO. The combined spectroscopic and computational studies suggest that the metallic CoFe alloy is the active phase responsible for producing C_{2+} hydrocarbons from the CO intermediate, whose formation is facilitated by the iron oxide surface sites generated *in situ* during the CO_2 hydrogenation reaction. The Na-modified CoFe alloy phase has an intermediate chain propagation activity, which promotes the C–C coupling reaction and enables high C_8–C_{16} selectivity. In addition, the introduction of Na and formation of the CoFe alloy structure effectively suppress CO_2 methanation. Therefore, our knowledge of the intricate reaction network involved in CO_2-based FTS is improved by these experimental and theoretical findings, which can

potentially facilitate the rational development of efficient materials for the direct hydrogenation of CO_2 to advanced liquid fuels.

REFERENCES

1. Patterson, B.D., Mo, F., Borgschulte, A., et al. (2019). Renewable CO_2 recycling and synthetic fuel production in a marine environment. Proc. Natl. Acad. Sci. U S A ***116***, 12212–12219.
2. Wei, J., Ge, Q., Yao, R., et al. (2017). Directly converting CO_2 into a gasoline fuel. Nat. Commun. ***8***, 15174.
3. Gao, P., Li, S.G., Bu, X.N., et al. (2017). Direct conversion of CO_2 into liquid fuels with high selectivity over a bifunctional catalyst. Nat. Chem. ***9***, 1019–1024.
4. Wang, X.X., Zeng, C.Y., Gong, N.N., et al. (2021). Effective suppression of CO selectivity for CO_2 hydrogenation to high-quality gasoline. ACS Catal. ***11***, 1528–1547.
5. Noreen, A., Li, M.Q., Fu, Y.J., et al. (2020). One-pass hydrogenation of CO_2 to multi-branched isoparaffins over bifunctional zeolite-based catalysts. ACS Catal. ***10***, 14186–14194.
6. Gao, P., Zhang, L.N., Li, S.G., et al. (2020). Novel heterogeneous catalysts for CO_2 hydrogenation to liquid fuels. ACS Cent. Sci. ***6***, 1657–1670.
7. Yao, B., Xiao, T., Makgae, O.A., et al. (2020). Transforming carbon dioxide into jet fuel using an organic combustion-synthesized Fe-Mn-K catalyst. Nat. Commun. ***11***, 6395.
8. Vogt, C., Monai, M., Kramer, G.J., and Weckhuysen, B.M. (2019). The renaissance of the sabatier reaction and its applications on Earth and in space. Nat. Catal. ***2***, 188–197.
9. Zhou, W., Cheng, K., Kang, J.C., et al. (2019). New horizon in C1 chemistry: breaking the selectivity limitation in transformation of syngas and hydrogenation of CO_2 into hydrocarbon chemicals and fuels. Chem. Soc. Rev. ***48***, 3193–3228.
10. Yang, D.X., Zhu, Q.G., and Han, B.X. (2020). Electroreduction of CO_2 in ionic liquid-based electrolytes. Innovation ***1***, 100016. https://doi.org/10.1016/j.xinn.2020.100016.
11. Bao, J., Yang, G.H., Yoneyama, Y., and Tsubaki, N. (2019). Significant advances in C1 catalysis: highly efficient catalysts and catalytic reactions. ACS Catal. ***9***, 3026–3053.
12. Rodemerck, U., Holena, M., Wagner, E., et al. (2013). Catalyst development for CO_2 hydrogenation to fuels. ChemCatChem ***5***, 1948–1955.
13. Choi, Y.H., Jang, Y.J., Park, H., et al. (2017). Carbon dioxide Fischer-Tropsch synthesis: a new path to carbon-neutral fuels. Appl. Catal. B ***202***, 605–610.
14. Guo, L.S., Sun, J., Ge, Q.J., and Tsubaki, N. (2018). Recent advances in direct catalytic hydrogenation of carbon dioxide to valuable C_{2+} hydrocarbons. J. Mater. Chem. A ***6***, 23244–23262.
15. Ramirez, A., Gevers, L., Bavykina, A., et al. (2018). Metal organic framework-derived iron catalysts for the direct hydrogenation of CO_2 to short chain olefins. ACS Catal. ***8***, 9174–9182.
16. Dorner, R.W., Hardy, D.R., Williams, F.W., and Willauer, H.D. (2010). Heterogeneous catalytic CO_2 conversion to value-added hydrocarbons. Energy Environ. Sci. ***3***, 884–890.
17. Guo, L., Sun, J., Ji, X., et al. (2018). Directly converting carbon dioxide to linear α-olefins on bio-promoted catalysts. Commun. Chem. ***1***, 11.
18. Gnanamani, M.K., Jacobs, G., Hamdeh, H.H., et al. (2016). Hydrogenation of carbon dioxide over Co-Fe bimetallic catalysts. ACS Catal. ***6***, 913–927.
19. Zhu, J., Zhang, G., Li, W., et al. (2020). Deconvolution of the particle size effect on CO_2 hydrogenation over iron-based catalysts. ACS Catal. ***10***, 7424–7433.
20. Xu, Y., Zhai, P., Deng, Y., et al. (2020). Highly selective olefin production from CO_2 hydrogenation on iron catalysts: a Subtle Synergy between Manganese and Sodium Additives. Angew. Chem. Int. Ed. Engl. ***59***, 21736–21744.
21. Li, Z.H., Liu, J.J., Shi, R., et al. (2021). Fe-based catalysts for the direct photohydrogenation of CO_2 to value-added hydrocarbons. Adv. Energy Mater. ***11***, 2002783.
22. Choi, Y.H., Ra, E.C., Kim, E.H., et al. (2017). Sodium-containing spinel zinc ferrite as a catalyst precursor for the selective synthesis of liquid hydrocarbon fuels. ChemSusChem ***10***, 4764–4770.
23. Li, J., He, Y.L., Tan, L., et al. (2018). Integrated tuneable synthesis of liquid fuels via Fischer-Tropsch technology. Nat. Catal. ***1***, 787–793.
24. Khodakov, A.Y., Chu, W., and Fongarland, P. (2007). Advances in the development of novel cobalt Fischer-Tropsch catalysts for synthesis of long-chain hydrocarbons and clean fuels. Chem. Rev. ***107***, 1692–1744.
25. de Smit, E., and Weckhuysen, B.M. (2008). The renaissance of iron-based Fischer-Tropsch synthesis: on the multifaceted catalyst deactivation behaviour. Chem. Soc. Rev. ***37***, 2758–2781.
26. Zhang, Y.Q., Jacobs, G., Sparks, D.E., et al. (2002). CO and CO_2 hydrogenation study on supported cobalt Fischer-Tropsch synthesis catalysts. Catal. Today ***71***, 411–418.
27. Owen, R.E., Plucinski, P., Mattia, D., et al. (2016). Effect of support of Co-Na-Mo catalysts on the direct conversion of CO_2 to hydrocarbons. J. CO2 Util. ***16***, 97–103.
28. Shi, Z.B., Yang, H.Y., Gao, P., et al. (2018). Effect of alkali metals on the performance of $CoCu/TiO_2$ catalysts for CO_2 hydrogenation to long-chain hydrocarbons. Chin. J. Catal. ***39***, 1294–1302.
29. He, Z.H., Cui, M., Qian, Q.L., et al. (2019). Synthesis of liquid fuel via direct hydrogenation of CO_2. P. Natl. Acad. Sci. U S A ***116***, 12654–12659.
30. Kim, K.Y., Lee, H., Noh, W.Y., et al. (2020). Cobalt ferrite nanoparticles to form a catalytic Co–Fe alloy carbide phase for selective CO_2 hydrogenation to light olefins. ACS Catal. ***10***, 8660–8671.
31. Gnanamani, M.K., Hamdeh, H.H., Jacobs, G., et al. (2017). Hydrogenation of carbon dioxide over K-promoted FeCo bimetallic catalysts prepared from mixed metal oxalates. ChemCatChem ***9***, 1303–1312.
32. Numpilai, T., Witoon, T., Chanlek, N., et al. (2017). Structure activity relationships of Fe-Co/K-Al2O3 catalysts calcined at different temperatures for CO_2 hydrogenation to light olefins. Appl. Catal. A ***547***, 219–229.
33. Satthawong, R., Koizumi, N., Song, C.S., and Prasassarakich, P. (2015). Light olefin synthesis from CO_2 hydrogenation over K-promoted Fe-Co bimetallic catalysts. Catal. Today ***251***, 34–40.
34. Jiang, F., Liu, B., Geng, S.S., et al. (2018). Hydrogenation of CO_2 into hydrocarbons: enhanced catalytic activity over Fe-based Fischer-Tropsch catalysts. Catal. Sci. Technol. ***8***, 4097–4107.
35. Hwang, S.M., Han, S.J., Park, H.G., et al. (2021). Atomically Alloyed Fe–Co Catalyst derived from a N-coordinated Co single-atom structure for CO_2 hydrogenation. ACS Catal. ***11***, 2267–2278.
36. Ismail, A.S.M., Casavola, M., Liu, B.Y., et al. (2019). Atomic-scale investigation of the structural and electronic properties of cobalt-iron bimetallic Fischer-Tropsch catalysts. ACS Catal. ***9***, 7998–8011.
37. Chen, G.B., Gao, R., Zhao, Y.F., et al. (2018). Alumina-Supported CoFe Alloy Catalysts derived from layered-double-hydroxide nanosheets for efficient photothermal CO_2 hydrogenation to hydrocarbons. Adv. Mater. ***30***, 1704663.
38. Yang, H.Y., Zhang, C., Gao, P., et al. (2017). A review of the catalytic hydrogenation of carbon dioxide into value-added hydrocarbons. Catal. Sci. Technol. ***7***, 4580–4598.
39. Pour, A.N., Khodabandeh, H., Izadyar, M., and Housaindokht, M.R. (2013). Mechanistic double ASF product distribution study of Fischer-Tropsch synthesis on precipitated iron catalyst. J. Nat. Gas. Sci. Eng. ***15***, 53–58.
40. Gaube, J., and Klein, H.F. (2008). Studies on the reaction mechanism of the Fischer-Tropsch synthesis on iron and cobalt. J. Mol. Catal. A Chem. ***283***, 60–68.
41. Hwang, S.M., Zhang, C.D., Han, S.J., et al. (2020). Mesoporous carbon as an effective support for Fe catalyst for CO_2 hydrogenation to liquid hydrocarbosns. J. CO2 Util. ***37***, 65–73.
42. Khan, M.K., Butolia, P., Jo, H., et al. (2020). Selective conversion of carbon dioxide into liquid hydrocarbons and long-chain α-olefins over fe-amorphous AlO_x bifunctional catalysts. ACS Catal. ***10***, 10325–10338.
43. Satthawong, R., Koizumi, N., Song, C.S., and Prasassarakich, P. (2013). Bimetallic Fe-Co catalysts for CO_2 hydrogenation to higher hydrocarbons. J. CO2 Util. ***3-4***, 102–106.
44. He, S., An, Z., Wei, M., et al. (2013). Layered double hydroxide-based catalysts: nanostructure design and catalytic performance. Chem. Commun. ***49***, 5912–5920.
45. del Arco, M., Trujillano, R., and Rives, V. (1998). Cobalt-iron hydroxycarbonates and their evolution to mixed oxides with spinel structure. J. Mater. Chem. ***8***, 761–767.
46. Wang, W., Wang, S.P., Ma, X.B., and Gong, J.L. (2011). Recent advances in catalytic hydrogenation of carbon dioxide. Chem. Soc. Rev. ***40***, 3703–3727.
47. Biesinger, M.C., Payne, B.P., Grosvenor, A.P., et al. (2011). Resolving surface chemical states in XPS analysis of first row transition metals, oxides and hydroxides: Cr, Mn, Fe, Co and Ni. Appl. Surf. Sci. ***257***, 2717–2730.
48. Mcintyre, N.S., and Zetaruk, D.G. (1977). X-Ray photoelectron spectroscopic studies of iron-oxides. Anal. Chem. ***49***, 1521–1529.
49. Zhu, M.H., and Wachs, I.E. (2016). Iron-based catalysts for the high-temperature water gas shift (HT-WGS) reaction: a Review. ACS Catal. ***6***, 722–732.
50. Yao, Z.H., Guo, C.X., Mao, Y., and Hu, P. (2019). Quantitative determination of C-C coupling mechanisms and detailed analyses on the activity and selectivity for Fischer-Tropsch synthesis on Co(0001): Microkinetic modeling with coverage effects. ACS Catal. ***9***, 5957–5973.
51. Chen, C., Wang, Q., Wang, G., et al. (2016). Mechanistic insight into the C2 hydrocarbons formation from syngas on fcc-Co(111) surface: a DFT study. J. Phsy. Chem. C ***120***, 9132–9147.
52. Yang, C., Liu, S., Wang, Y., et al. (2019). The interplay between structure and product selectivity of CO2 hydrogenation. Angew. Chem. Int. Ed. Engl. ***58***, 11242–11247.
53. Wang, S.G., Temel, B., Shen, J.A., et al. (2011). Universal bronsted-evans-polanyi relations for C-C, C-O, C-N, N-O, N-N, and O-O dissociation reactions. Catal. Lett. ***141***, 370–373.

ACKNOWLEDGMENTS

We thank Dr. Alexander van der Made and Dr. Joost Smits for helpful discussions. X-Ray absorption studies were performed at the BL11B beamline at the Shanghai Synchrotron Radiation Facility (SSRF), Shanghai, PR China. This work was financially supported by the "Frontier Science" program of Shell Global Solutions International B.V. (PT65197), the National Natural Science Foundation of China (21773286, U1832162), the Strategic Priority Research Program of the Chinese Academy of Sciences (XDA21090204), the Youth Innovation

Promotion Association CAS (2018330), and the Shanghai Rising Star Program, China (19QA1409900).

AUTHOR CONTRIBUTIONS

P.G. and Y.S. conceived the project. P.G. and S.L. analyzed the data and wrote the paper. P.G., L.Z., Y.D., X.Z., A.B., and H.W. drafted the manuscript. L.Z. prepared various materials. L.Z. and H.W. performed sample characterization and catalytic evaluation. X.Z., E.V., and Y.Y. did the *in situ* XPS experiments and analysis. Y.D., L.S., Y.G., and S.L. performed the DFT calculations. All authors discussed the experimental and theoretical results and commented on the manuscript.

DECLARATION OF INTERESTS

The authors declare no competing interests.

LEAD CONTACT WEBSITE

https://www.researchgate.net/profile/Peng-Gao-15.

SUPPLEMENTAL INFORMATION

Supplemental information can be found online at https://doi.org/10.1016/j.xinn.2021.100170.

The Innovation, Volume *2*

Supplemental Information

Direct conversion of CO_2 to a jet fuel over CoFe alloy catalysts

Lei Zhang, Yaru Dang, Xiaohong Zhou, Peng Gao, Alexander Petrus van Bavel, Hao Wang, Shenggang Li, Lei Shi, Yong Yang, Evgeny I. Vovk, Yihao Gao, and Yuhan Sun

Supplemental Materials and Methods

Catalyst preparation. CoFe-*x*Na catalysts prepared from CoFe-LDH materials were synthesized with atomic ratios of Co^{2+}:Fe^{3+} = 2. All the LDH precursors were fabricated by co-precipitation at room temperature. The mixed solution of Co/Fe nitrate salts (0.5 mol L^{-1}) and the mixed solution of Na_2CO_3 and NaOH (1 mol L^{-1}) were added simultaneously, and the pH value was controlled in 10. After the precipitate was aged for 15 hours at 70°C, the filter cake was obtained by centrifugation and washing. Derived product was placed in the oven at 100 ºC for 14 h to obtain various CoFe-LDH samples. The CoFe-*x*Na catalysts were prepared by calcination of the corresponding precursors in muffle furnace at 500 ºC for 4 h. The sodium concentration of CoFe-*x*Na catalysts was controlled by adjusting the total amounts of water during filtration and washing steps. CoFe-LDH precursors of CoFe-0.81Na were suspended in DMF and placed in an ultrasonic bath under stirring. Samples were sonicated for 6 h and then filtered and calcined at 500 ºC to obtain CoFe-0.82Na-U. Co-0.63Na, Co, Fe-0.67Na, Fe and CoFe/Al_2O_3-1.09Na catalysts were synthesized without the iron or cobalt nitrite solution or with the aluminum nitrite solution (Co^{2+}:Fe^{3+}:Al^{3+} = 2:1:0.6) at otherwise the same conditions. Pure CoFe, Co and Fe samples were obtained by washing the precursors 50 times before calcination.

Catalyst characterization. The metal composition of various samples was analyzed by an inductively coupled plasma-optical emission spectroscopy (Thermo iCAP 6300). XRD spectra of samples were collected on Rigatku Ultima 4 X-ray diffractometer utilizing Cu Kα radiation. Surface areas were obtained from N_2 adsorption at –196 ºC. Scanning electron microscopy (SEM, SUPRRATM 55), TEM and high-resolution TEM (HRTEM, FEI Tecnai G2 F20) investigations were performed to reveal the morphology of the materials. Scanning TEM (STEM) and EDX studies were also did on a FEI Tecnai

G2 F20 microscope with an Oxford EDX detector. The Co and Fe K-edge XAFS data were recorded on the BL11B beamline of Shanghai Synchrotron Radiation Facility at 25 ºC, operated with the electron beam energy of 2.5 GeV and the current of 200 mA. H_2–TPR and CO_2/H_2/CO–TPD measurements were performed on a Micromeritics ChemiSorb 2920. The H_2/CO and CO_2 signals were detected by a thermal conductivity detector (TCD) and mass spectrometer (OmniStar GSD320 02), respectively. For H_2–TPR, the 100 mg catalyst is treated in Ar gas at 150 ºC for 1 h, and then placed in the 5%H_2/95%Ar mixture at 50 ºC. After the baseline is stabilized, the temperature was programmed to rise to 750 ºC. For CO_2−TPD, after pretreatment of the material, a CO_2 flow was continued at 50 ºC for 1.5 h. Switch the Ar gas to purge until the CO_2 signal (m/z = 44) is stable at 50 ºC, and then heat up to 500 ºC. For H_2/CO–TPD, firstly, the material was reduced with H_2 at 400 ºC for 6 h and then flushed with inert gas for 1 h at 400 ºC and cooled to 50 ºC. A pure H_2 or CO flow was continued for 1 h at 50 ºC and the desorption of H_2 or CO was conducted from 50 to 750 ºC under pure Ar. The X-Ray absorption spectra (XAS) were recorded at the BL11B beamline of Shanghai Synchrotron Radiation Facility (SSRF). The beam current of the storage ring was 220 mA in a top-up mode. The incident photons were monochromatized by a Si(111) double-crystal monochromator, with an energy resolution $\Delta E/E \sim 1.4 \times 10^{-4}$. The rejection of higher harmonics was achieved by a pair of Cr-coated mirrors at 4 mrad. The spot size at the sample was ~200 μm × 250 μm (H × V). The XAS spectra were recorded in the transmission mode. The *in situ* DRIFTS were collected by a Nicolet 6700 infrared spectrometer equipped with a cylindrical cavity cell and MCT detector. Before DRIFTS analyses, catalysts (30 mg) undergone the same reduction pretreatment in the cell as the H_2/CO–TPD process, which were then cooled down to the target temperatures under Ar and the corresponding background spectra at different temperatures (50, 100, 150, 200 and 240 ºC) were collected for subsequent DRIFTS

analyses. After that, the flow of Ar was switched to pure CO_2 at 50 ºC, and IR spectra were recorded when increased severe specific temperatures (50−240 ºC) for 10 mins. After CO_2 flow at 240 ºC for 40 min, the H_2 stream was introduced into the cylindrical cavity cell. IR spectra were recorded for CO_2 hydrogenation at 240 ºC and specific times in the range of 1−60 min. XPS experiments were performed in a ThermoFischer photoelectron spectrometer (ESCALAB 250Xi) equipped with non-monochromatic X-ray Irradiation Mg Kα (hv = 1253.6 eV). The device was also equipped with a 180° double focusing hemispherical analyzer with a six-channel detector. The Mg Kα source was chosen since under Al Kα irradiation there is strong overlapping of Co 2p photoemission spectrum with Fe LMM Auger peaks and overlapping of Fe 2p spectrum with Co LMM Auger peaks which makes the spectra analysis very difficult. The C 1s peak located at 284.9 eV associated with adventitious carbon was used to calibrate all XPS peak spectra. *In situ* reduction and subsequent reaction over the catalyst were performed in an ultra-high vacuum connected Fermi Model HPGC 300 high pressure gas cell. Typically, the calcined CoFe-0.81Na catalyst was first reduced in 0.1 MPa of H_2 at 400 ºC for 3 h. *In situ* CO_2 hydrogenation reaction was performed in 0.8 MPa CO_2 and H_2 for 5 h at 200 ºC or 240 ºC. XPS spectra were recorded after cooling of the sample in the correspond flow, pumping down and transfer to the analysis chamber of the spectrometer.

Catalytic evaluation. The mixture of catalyst (0.5 g) and the same volume of quartz sand was filled into a fixed bed reactor. Prior to reaction, the pure H_2 (0.5 MPa) was used to reduce the catalyst at 400 ºC for 6 h. Then, when the center temperature of catalyst bed was cooled down to target temperatures, the feed gas ($H_2/CO_2/N_2$) was introduced into the stainless-steel reactor. An online gas chromatograph equipped with a TCD and a hydrogen flam ionization detector (Agilent GC 7890A) was utilized to analyze the CO_2 hydrogenation products. The conversion of CO_2 and the selectivity of CO were

calculated using an internal normalization method. Hydrocarbon distributions are determined based on total carbon moles. The carbon balance was determined to be in the range of 96~104%. The evaluation data after running for 48 h was employed in this paper.

DFT calculations. DFT calculations were performed with the VASP program using the PBE functional with spin polarization. The projector-augmented wave (PAW) method was used with an energy cutoff of 400 eV. CoO, Co, and CoFe phases were modeled by the p(2×2) supercell with 4 atomic layers (ALs) for Co(100), the p(2×3) supercell with 4 ALs for Co(10-11), and the p(3×2) supercell with 5 ALs for Co/Fe(100), respectively, using the k-point grids of (7×7×1), (5×3×1), and (3×3×1). Models for the Na-promoted Co and CoFe phases are similar to those adopted in the literature.[1] Atoms in the top three atomic layers along with those in the adsorbate were fully relaxed with a force convergence of 0.05 eV/Å. Adjacent slabs were separated by a 20 Å vacuum region to avoid possible interaction between neighboring slabs. The transition state with four or more images was found using the climbing image nudged elastic band (CI-NEB) approach with four or more images. Charge density difference analysis was performed with VESTA by calculating the charge difference before and after the adsorption of an adsorbate.

Table S1. Metal compositions and textural properties of CoFe-*x*Na, Co-*x*Na and Fe-*x*Na catalysts.

Catalysts	Metal content (wt %)			Molar ratio	BET specific surface area ($m^2\ g^{-1}$)	BJH pore volume ($cm^3\ g^{-1}$)	Pore diameter (nm)
	Co	Fe	Na	Co/Fe			
$CoFe/Al_2O_3$-1.09Na	42.0	20.1	1.09	1.98	97	0.40	16.6
CoFe-0.82Na-U	47.1	22.5	0.83	1.98	66	0.15	12.1
CoFe-3.54 Na	45.1	22.2	3.54	1.93	54	0.30	22.1
CoFe-0.81Na	47.0	22.9	0.81	1.94	69	0.30	17.4
CoFe-0.23 Na	47.5	23.0	0.23	1.96	75	0.38	20.1
CoFe	47.2	23.4	0.01	1.91	585	0.22	14.9
Co-0.63 Na	70.5	−	0.63	−	50	0.23	18.6
Co	71.0	−	0.02	−	28	0.17	24.3
Fe-0.67 Na	−	69.7	0.67	−			
Fe	−	72.4	0.01	−			

CoFe without Na were obtained by washing precursors 50 times, which destroyed the LDH structure as shown by the much lower crystallinity of CoFe precursors (Figure S5A) and results in the decrease of specific surface areas. However, excessive amount of residual Na can block the channel of CoFe-3.54Na, which also decreases the BET surface area.

Table S2. Comparison of the catalytic performance of various catalysts for the CO_2 hydrogenation to C_8–C_{16} hydrocarbons.

Catalyst	Active site	P (MPa)	T (°C)	WHSV (mL g_{cat}^{-1} h^{-1})	H_2/CO_2	CO_2 Conv. (%)	CO Select. (%)	C_8–C_{16} Select. in HC (%)	C_8–C_{16} Yield [a]	Ref.
Fe-Mn-K	χ-Fe_5C_2	1	300	2400	3	38.2	5.6	47.8	65	[2]
Fe-Cu	χ-Fe_5C_2	1	300	1800	3	16.7	31.4	~37	12	[3]
Fe-Zn	χ-Fe_5C_2	1	340	1800 (7.69%N_2)	3	34	11.7	~49	35	[4]
FeK/Co-NC	Fe-Co mixed carbide	2.5	300	2000 (10%Ar)	3	54.6	~3	~30	40	[5]
CoFe-0.81Na	CoFe alloy	3	240	5500 (3%N_2)	3	10.2	5.2	63.5	51	This work

[a] Unit in mg g_{cat}^{-1} h^{-1}

Table S3. The catalytic performance of various catalysts in the CO_2 hydrogenation reaction.

Entry	Catalysts	Conv. (%)	CO Sel. (%)	Hydrocarbon distribution (C mol%)			
				CH_4	C_2–C_4	C_5–C_7	C_{8+}
1	CoFe-0.82Na-U	11.0	5.4	22.7	9.1	8.3	59.9
2	CoFe/Al_2O_3-1.09Na	37.2	0.3	33.9	16.5	9.9	39.7
3	Fe-0.67Na	5.0	59.2	17.2	23.2	15.5	44.1
4	Fe	9.1	4.5	50.9	41.1	1.2	6.8

Standard reaction conditions: $H_2/CO_2/N_2$ = 73/24/3, T = 240 °C, GHSV = 5500 mL·g^{-1}·h^{-1}, P = 3 MPa. The data is collected after 48 h time on stream.

The space-time yield of C_8–C_{16} over CoFe-0.81Na was found to be comparable to those of catalysts with carbides as the active phases at the much lower reaction temperature, though the CO_2 conversion is also lower (Table S2). In general, reducing the metal nanoparticle sizes or enhancing the metal dispersion can improve metal utilization efficiency and lead to higher activity for CO_2 hydrogenation.[6-9] To further increase the catalytic activity, we synthesized small CoFe-LDH nanosheets by using the reported ultrasonic method,[10] and obtaining CoFe-0.82Na-U after calcination. As shown in Table S3, the CoFe-0.82Na-U catalyst exhibits a similar catalytic performance to CoFe-0.81Na with a slightly higher CO_2 conversion. It is generally accepted that the introduction of supports such as Al_2O_3 can enhance the dispersion of metal nanoparticles and reduce their particle sizes. We also prepared CoFe/Al_2O_3-1.09Na with the Co/Fe molar ratio of 1.98 by using CoFeAl-LDH as the precursor. Compared with CoFe-0.81Na, the CO_2 conversion over CoFe/Al_2O_3-1.09Na amounts to 37.2% (Table S3, Entry 2), which is about 3.7-fold higher than that over CoFe-0.81Na, although C_{8+} selectivity decreases to 39.7% with a much higher CH_4 selectivity (33.9% vs 17.8%).

Table S4. Co K-edge EXAFS fitting results for CoFe-0.81Na catalysts and Co foil.[a]

Sample	Pair	CN	R (Å)	σ^2 (x 10^3)	ΔE_o (eV)
Co foil	Co−Co	12	2.50	6.94	6.0
CoFe-0.81Na-calcined	Co−O	1.2	1.90	3.09	2.55
	Co−Co	4.1	2.08	2.23	25.6
CoFe-0.81Na-reduced	Co−Fe	2.2	2.49	0.55	65.6
	Co−Co	2.1	2.47	0.53	20.2
CoFe-0.81Na-spent	Co−Fe	2.4	2.48	0.56	67.8
	Co−Co	2.3	2.47	0.53	20.8

[a] CN, coordination number; R, interatomic distance; σ^2, disorder parameter; ΔE_o, energy shift. All the fitting analysis were performed in the R space, $\Delta R = 1.0-3.5$ and $\Delta K = 2.0-11.2$.

Table S5. Fe K-edge EXAFS fitting results for CoFe-0.81Na catalysts and Fe foil.

Sample	Pair	CN	R (Å)	σ^2 (x 10^3)	ΔE_o (eV)
Fe foil	Fe−Fe	8	2.48	6.20	6.5
CoFe-0.81Na-calcined	Fe−O	0.5	1.96	1.04	2.96
	Fe−Fe	5.6	2.68	7.37	26.9
CoFe-0.81Na-reduced	Fe−Co	2.0	2.51	0.56	31.2
	Fe−Fe	2.3	2.46	1.66	59.4
CoFe-0.81Na-spent	Fe−Co	2.2	2.51	0.35	22.8
	Fe−Fe	2.5	2.49	1.65	62.4

Table S6. Energy barriers (E_a) and reaction energies (Δ_rE) in eV for CH_x (x = 1, 2) hydrogenation and coupling reactions on the Co(10-11) and CoFe(110) surfaces. The numbers in the parentheses are for the Na-promoted Co(10-11) and CoFe(110) surfaces.

Surface elementary steps	Co(10-11)		CoFe(110)	
	E_a	Δ_rE	E_a	Δ_rE
$CH^* + H^* \rightarrow CH_2 + *$	0.62 (0.64)	0.55 (0.57)	0.42 (0.62)	0.26 (0.40)
$CH_2^* + H^* \rightarrow CH_3^* + *$	0.53 (0.51)	−0.14 (−0.05)	0.57 (0.66)	−0.10 (0.15)
$CH^* + CH_2^* \rightarrow CHCH_2^* + *$	0.17 (0.31)	−0.25 (−0.15)	0.61 (0.86)	−0.01 (−0.07)
$CH_2^* + CH_2^* \rightarrow C_2H_4^* + *$	0.38 (0.25 [a])	−0.40 (−0.35)	0.51 (0.62)	−0.38 (−0.54)

[a] Estimated from the BEP relationship.

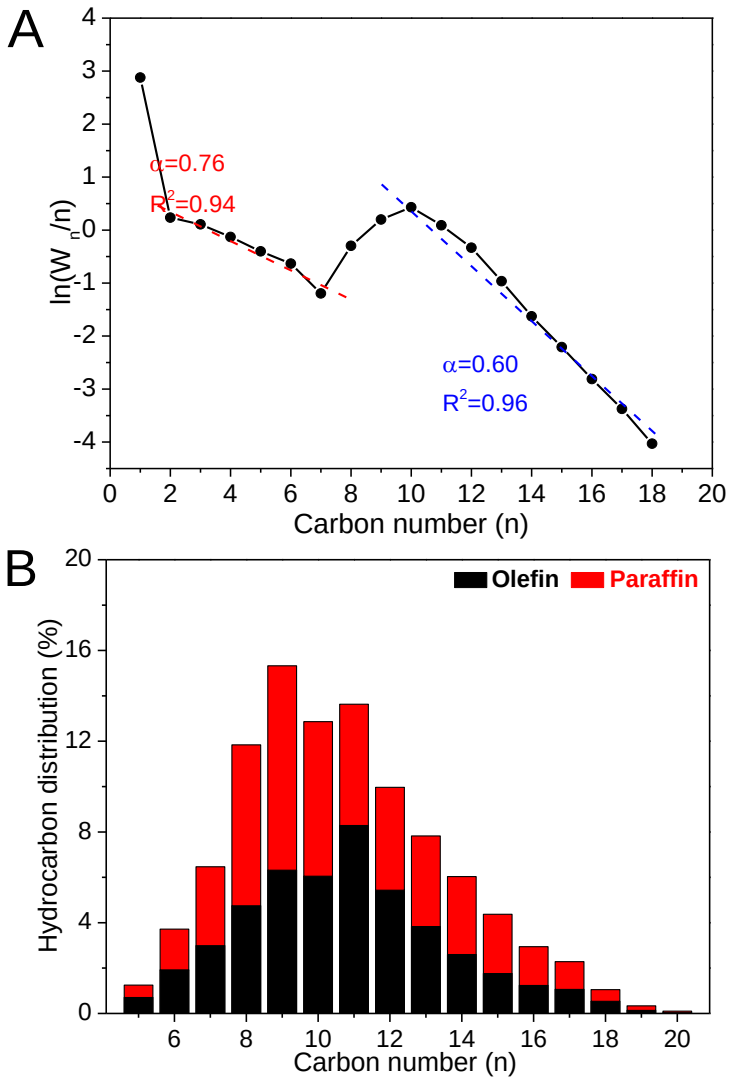

Figure S1. Hydrocarbon distribution for CO_2/CO hydrogenation (A) ASF plot and α values over the CoFe-0.81Na catalyst under the reaction condition shown in Table S3. W_n is the weight fraction of a hydrocarbon with *n* carbon atoms. (B) Hydrocarbon distribution of the liquid products of CO hydrogenation over the CoFe-0.81Na catalyst at $H_2/CO/N_2 = 73/24/3$, T = 240 ºC, GHSV = 5500 $mL \cdot g^{-1} \cdot h^{-1}$, P= 3 MPa.

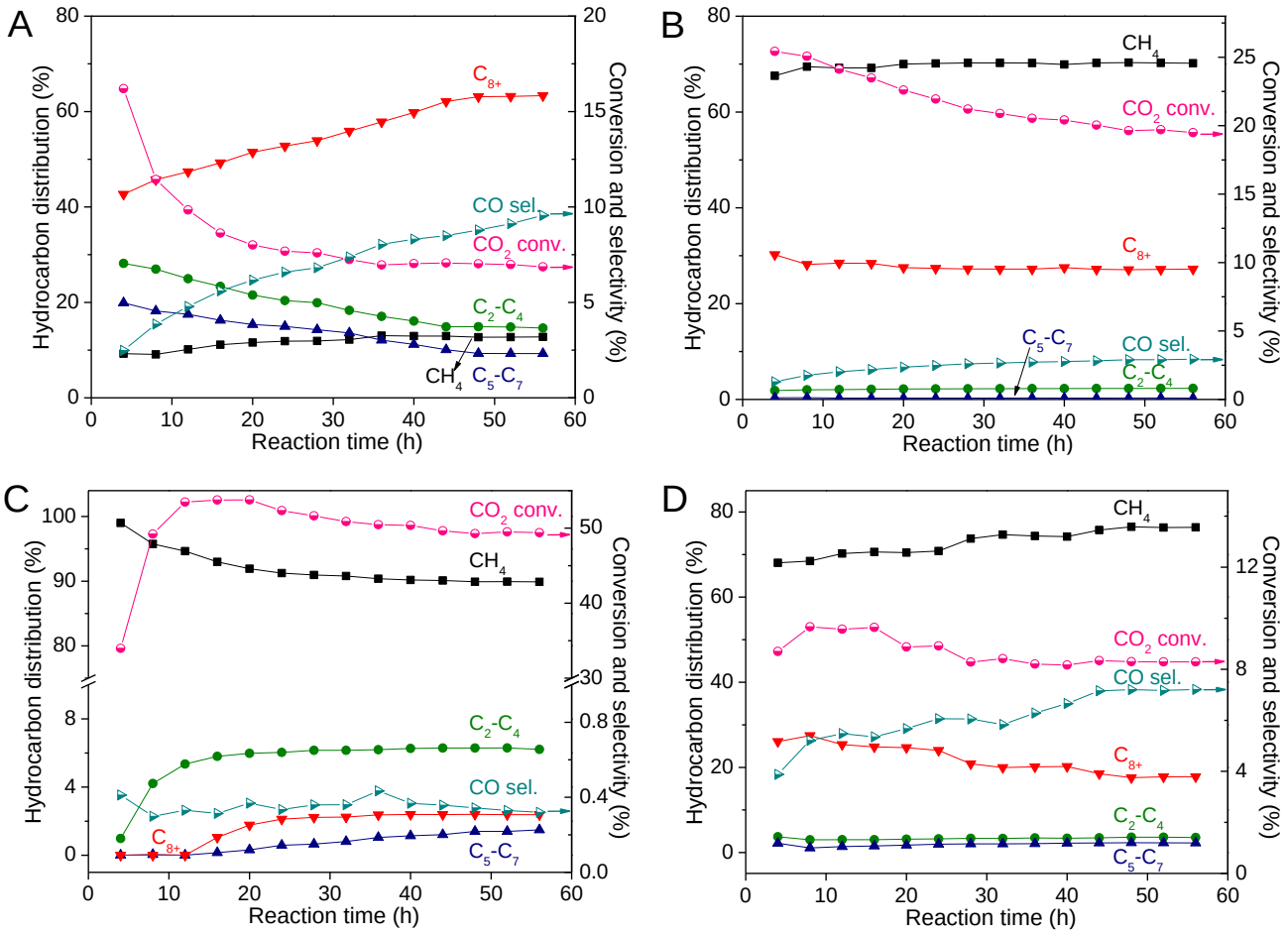

Figure S2. Catalytic stability (A−D) CO_2 hydrogenation performance of (A) CoFe-3.54Na, (B) CoFe, (C) Co and (D) Co-0.63Na catalysts with time-on-stream under standard reaction conditions.

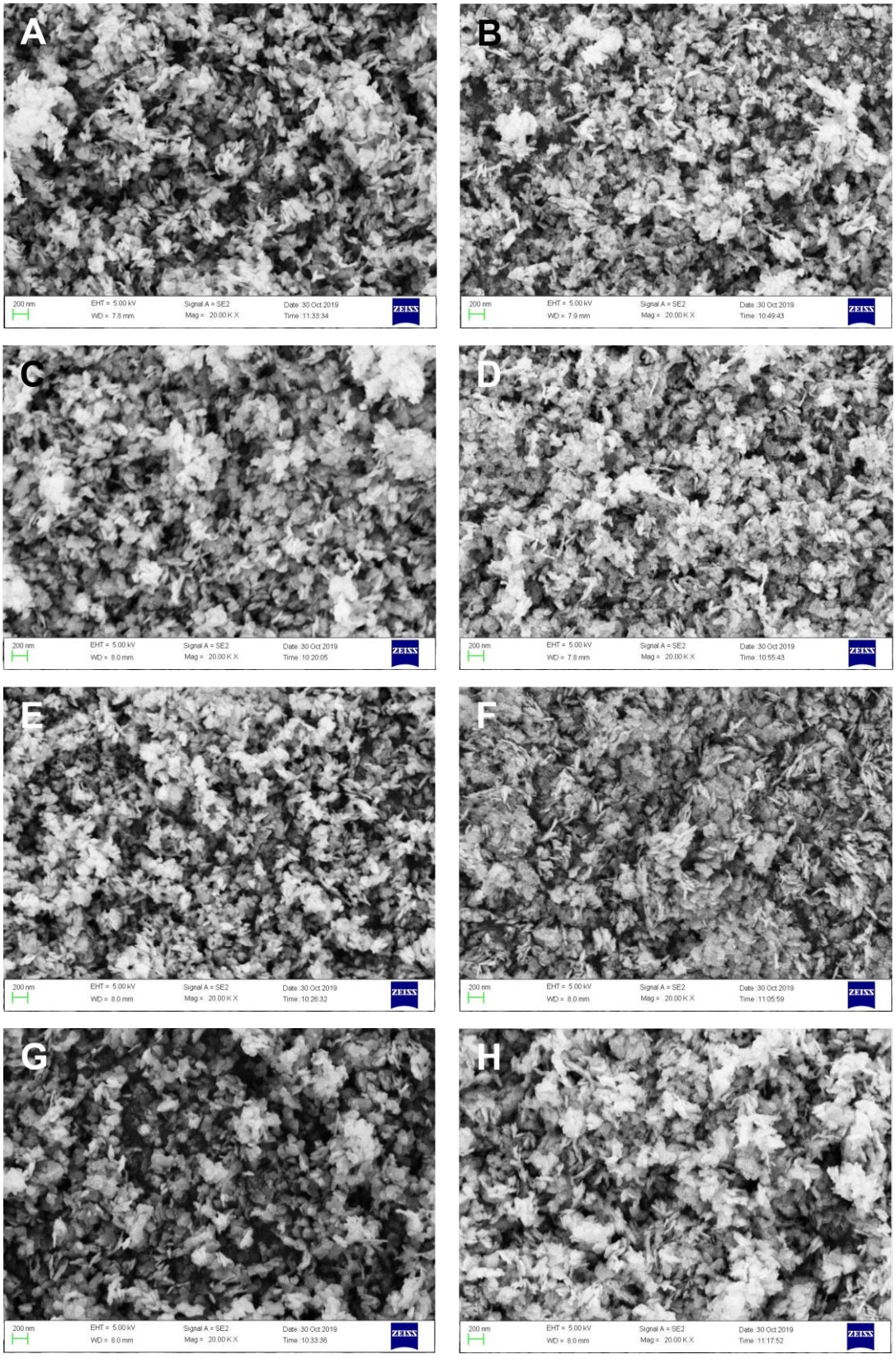

Figure S3. Morphology of uncalcined precursors and corresponding calcined samples SEM images of (A) CoFe, (C) CoFe-0.23Na, (E) CoFe-0.81Na and (G) CoFe-3.54Na precursors, as well as calcined (B) CoFe, (D) CoFe-0.23Na, (F) CoFe-0.81Na and (H) CoFe-3.54Na catalysts.

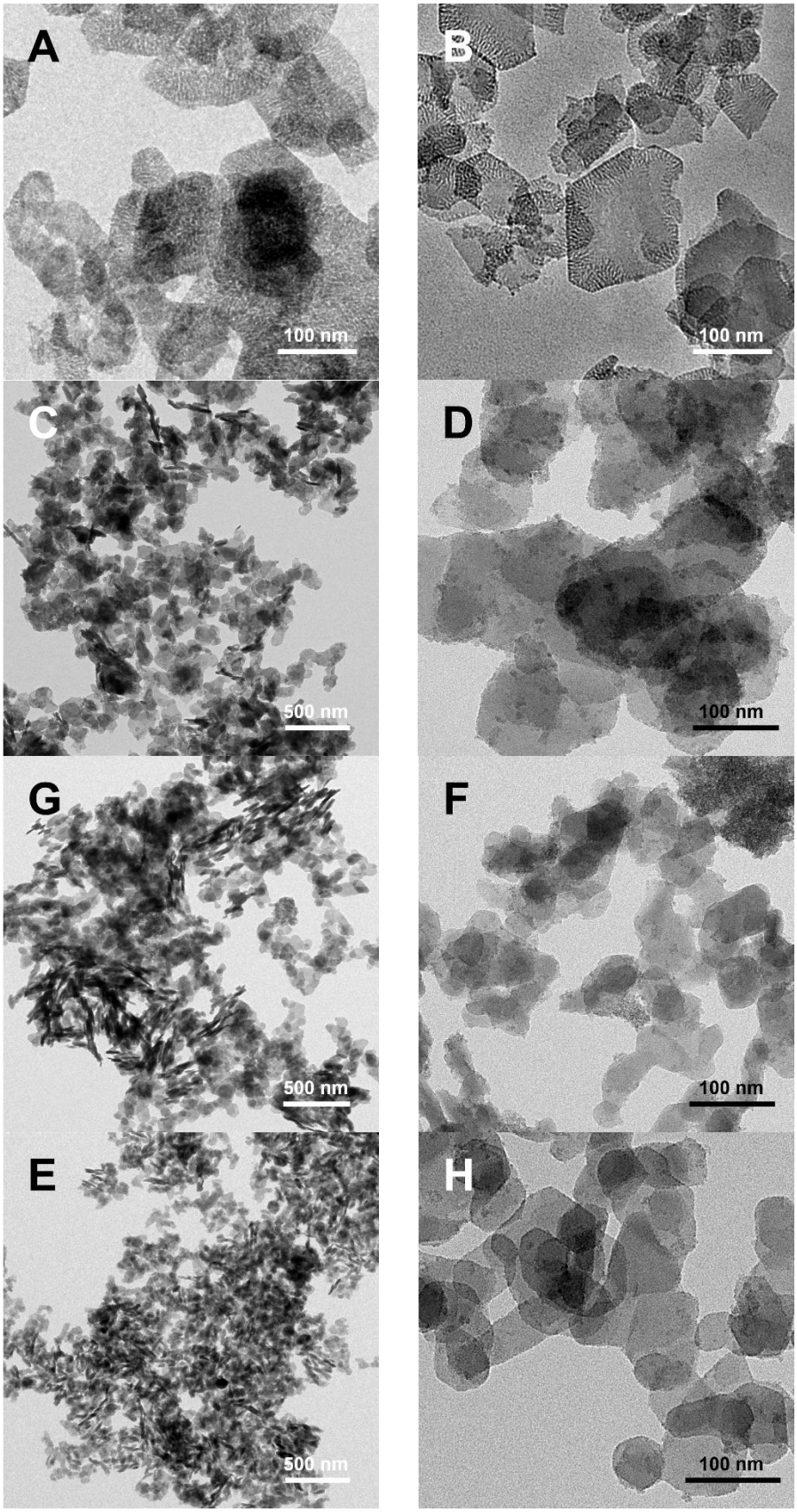

Figure S4. TEM images of (A) CoFe, (B) CoFe-0.81Na, (C and D) CoFe-3.54Na, (E and F) CoFe-0.82Na-U and (G and H) CoFe/Al_2O_3-1.09Na uncalcined precursors.

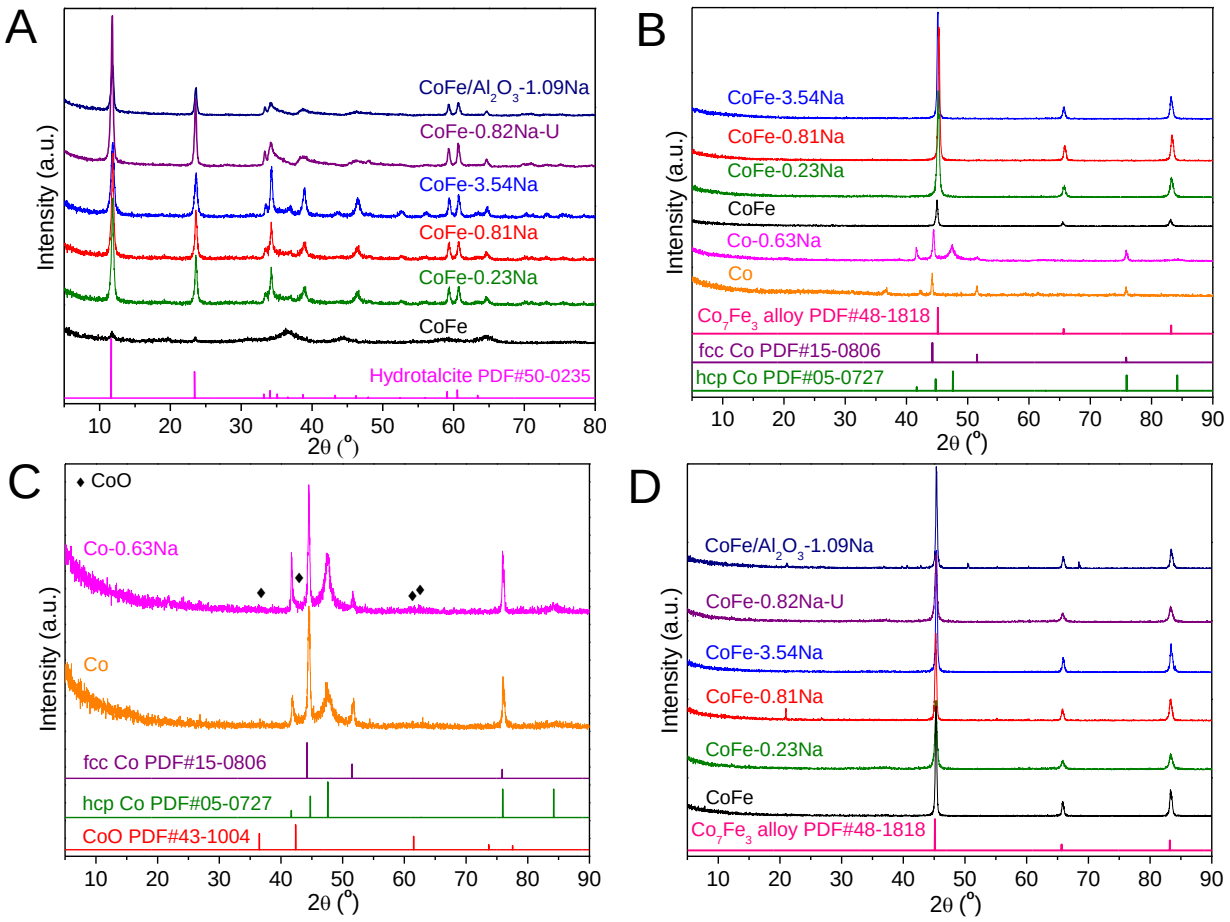

Figure S5. XRD patterns of (A) uncalcined precursors of various catalysts, as well as corresponding (B) reduced and (C and D) used samples.

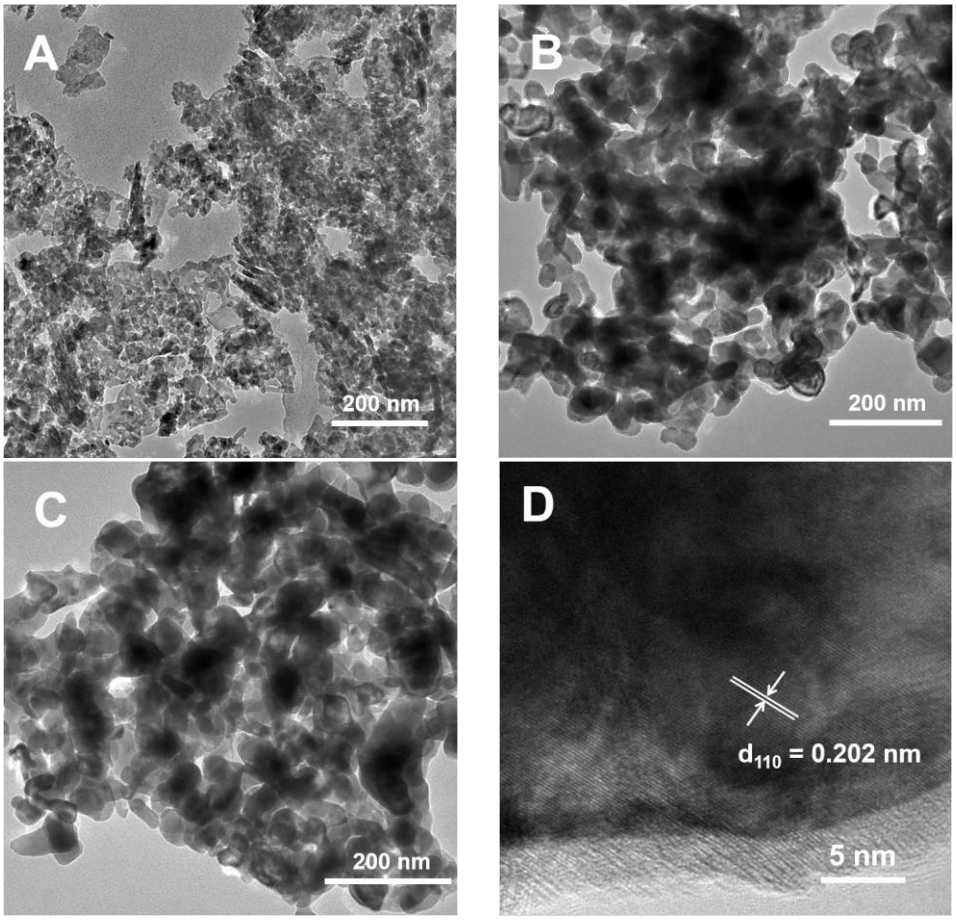

Figure S6. (A−E) TEM images of (A) calcined, (B) reduced and (C) used CoFe-0.81Na. (D) HRTEM images of used CoFe-0.81Na after CO_2 hydrogenation reaction.

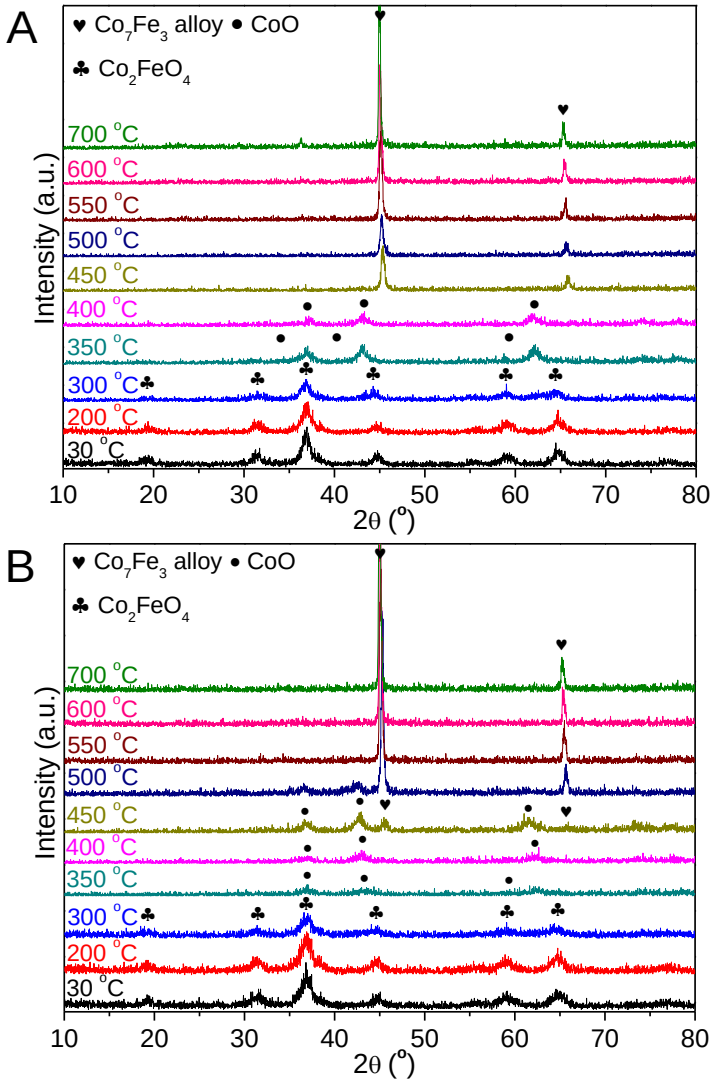

Figure S7. *In situ* XRD patterns of (**a**) CoFe-0.81Na and (**b**) CoFe-3.54Na obtained in 5% H_2/Ar with the increase of the temperature from 30 to 700 °C.

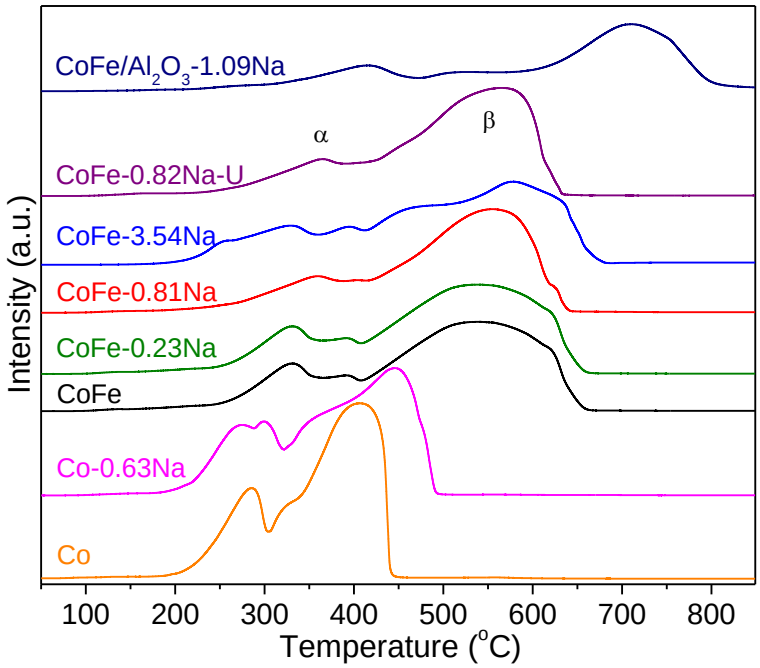

Figure S8. H_2−TPR profiles of various calcined samples.

From the H_2–TPR profiles (Figure S8), the high-temperature peaks (β peak) shift from around 560 °C for CoFe-*x*Na and CoFe-0.82Na-U to 716 °C for CoFe/Al_2O_3-1.09Na, suggesting that the introduction of the Al_2O_3 support remarkably decreases the reducibility of CoFe/Al_2O_3-1.09Na.

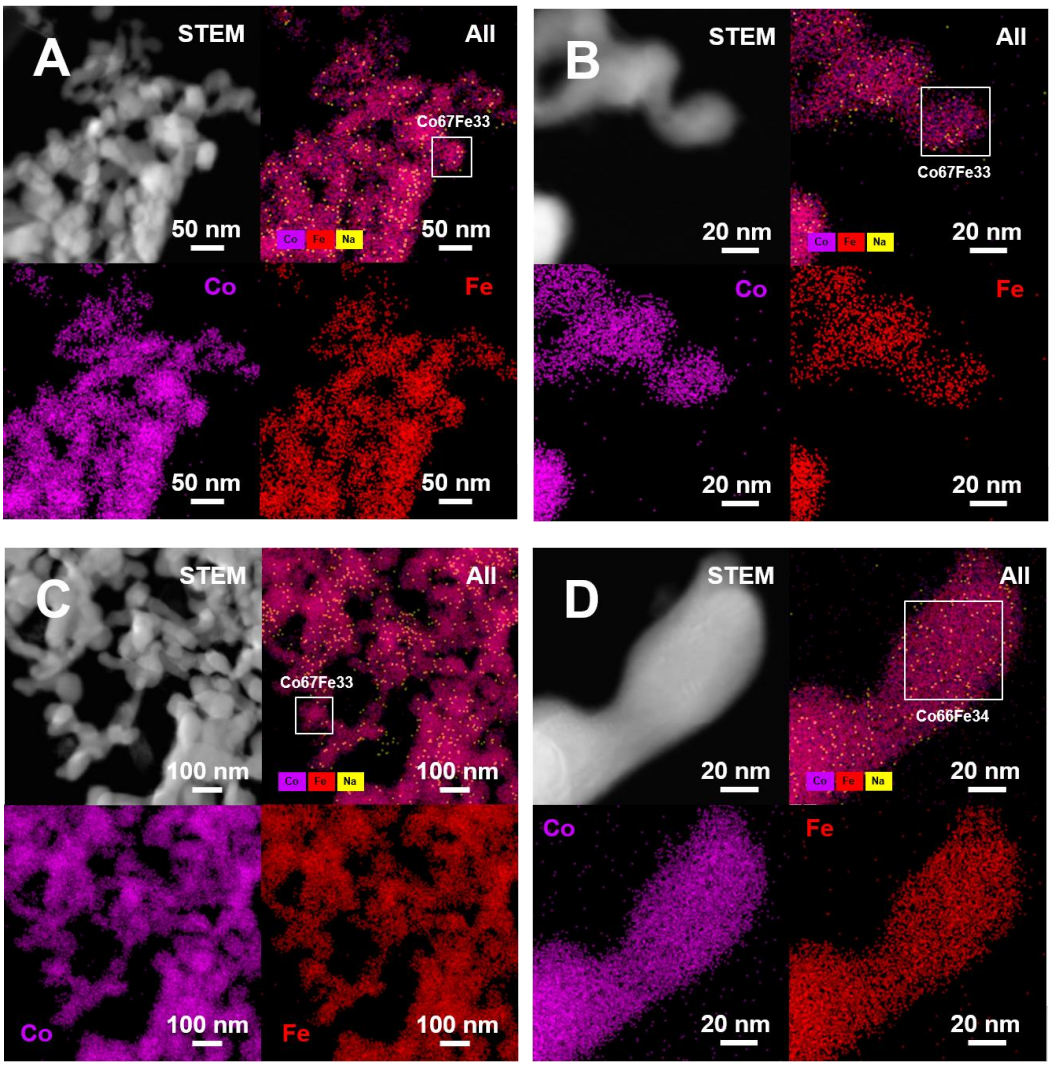

Figure S9. STEM-EDX images of reduced (A and B) CoFe-0.81Na and (C and D) CoFe-3.54Na catalysts. Co (magenta), Fe (red), Na (yellow).

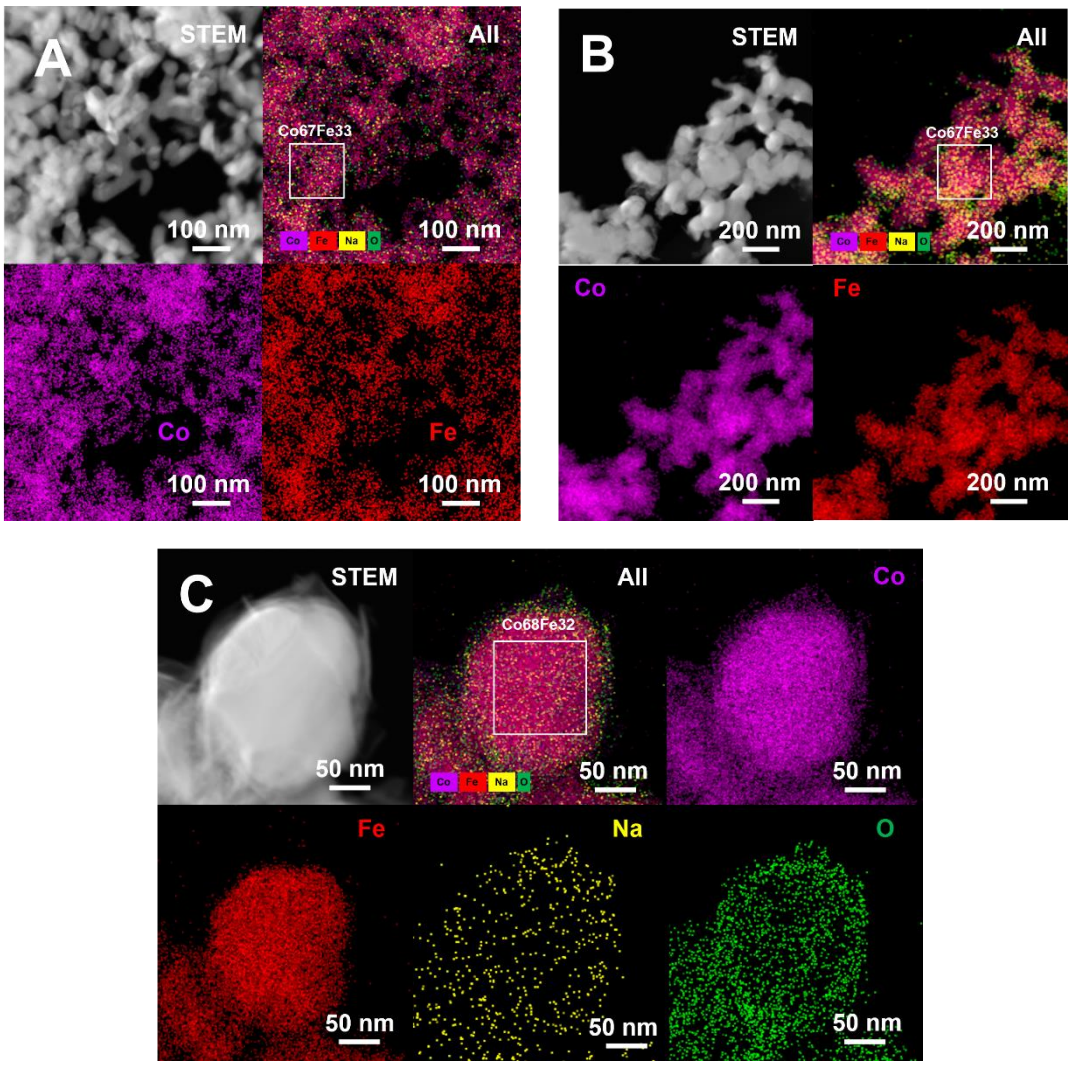

Figure S10. STEM-EDX images of spent (A) CoFe-0.81Na and (B and C) CoFe-3.54Na catalysts. Co (magenta), Fe (red), Na (yellow), O (green).

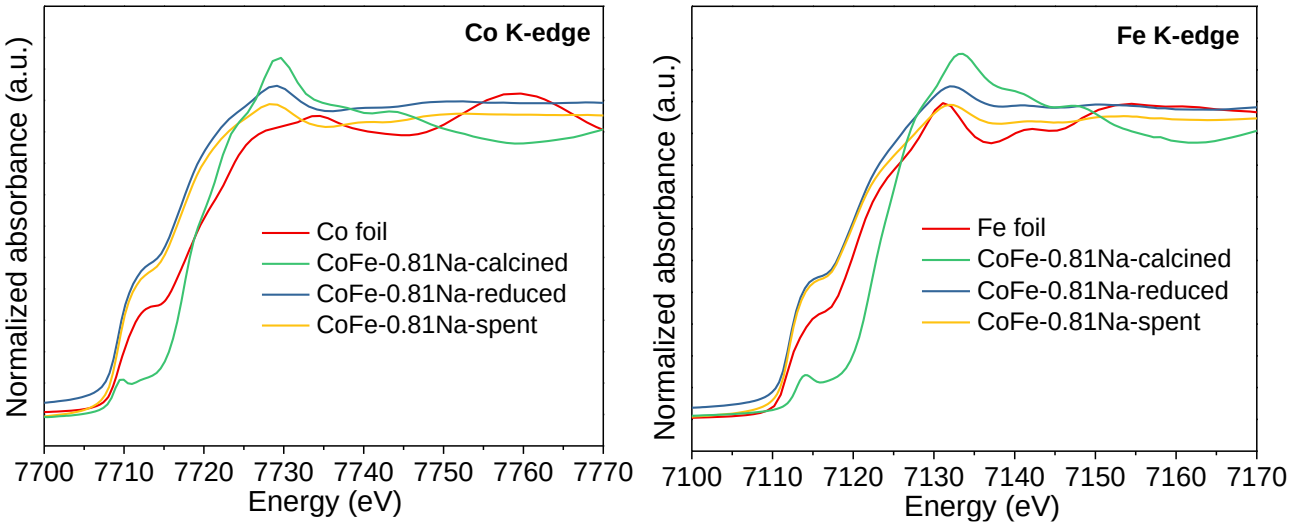

Figure S11. XANES spectra of the calcined, reduced and spent CoFe-0.81Na and reference samples at the Co and Fe K-edge.

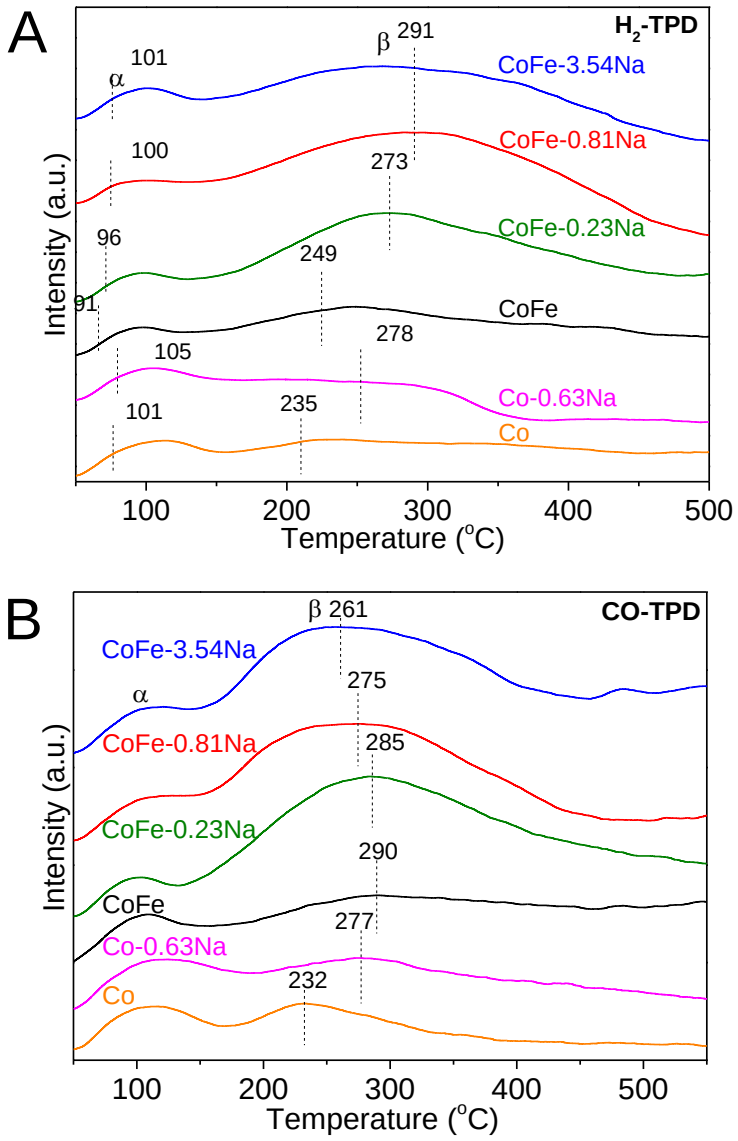

Figure S12. H_2/CO−TPD characterizations (A) H_2−TPD and (B) CO−TPD profiles over various catalysts.

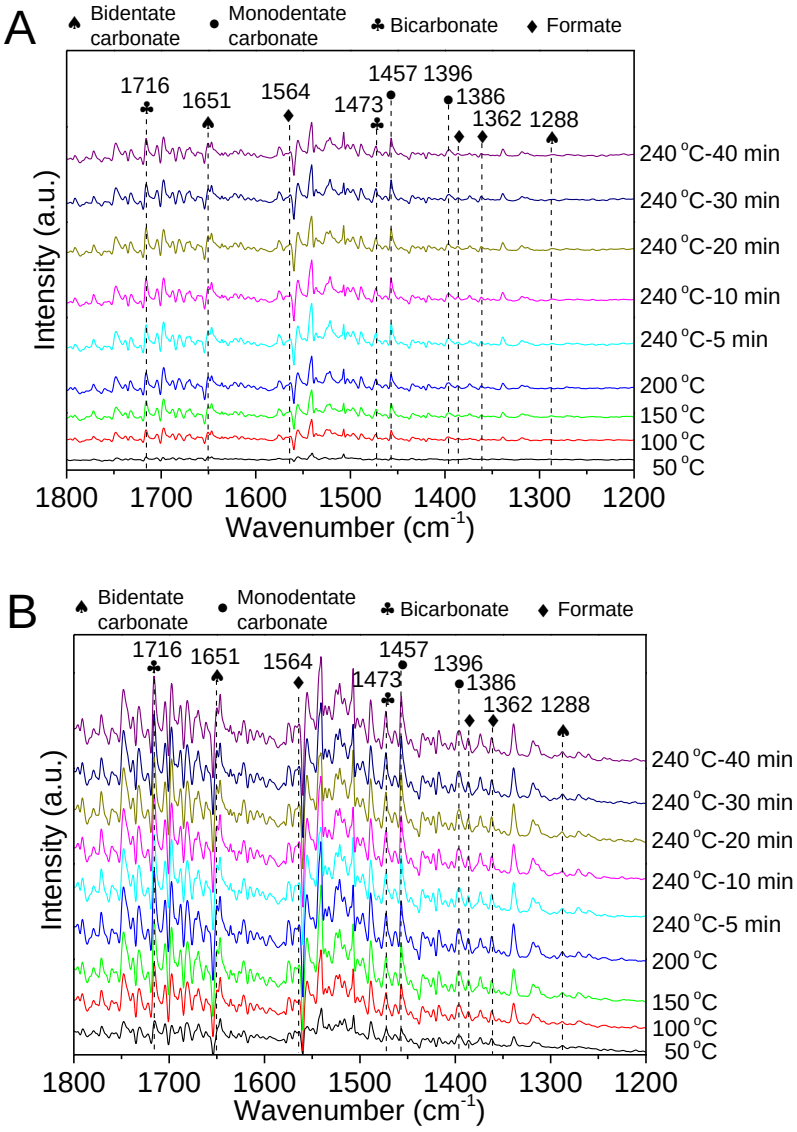

Figure S13. *In situ* DRIFTS analysis of (A) Co and (B) CoFe catalysts during CO_2 adsorption were collected at different temperature and times.

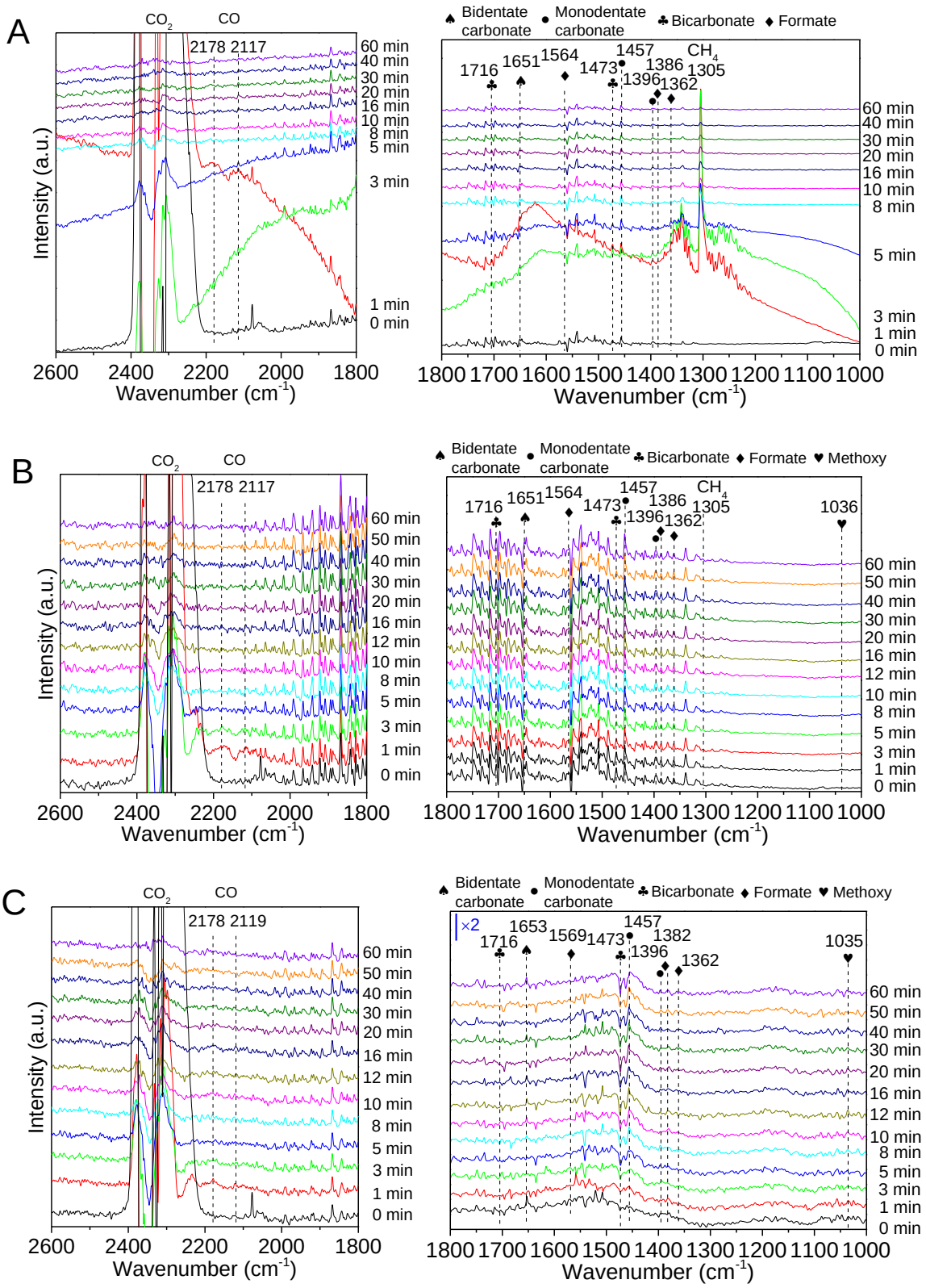

Figure S14. *In situ* DRIFTS analysis of (A) Co, (B) CoFe, and (C) CoFe-0.81Na catalysts during CO_2 hydrogenation were collected at 240 °C and different times.

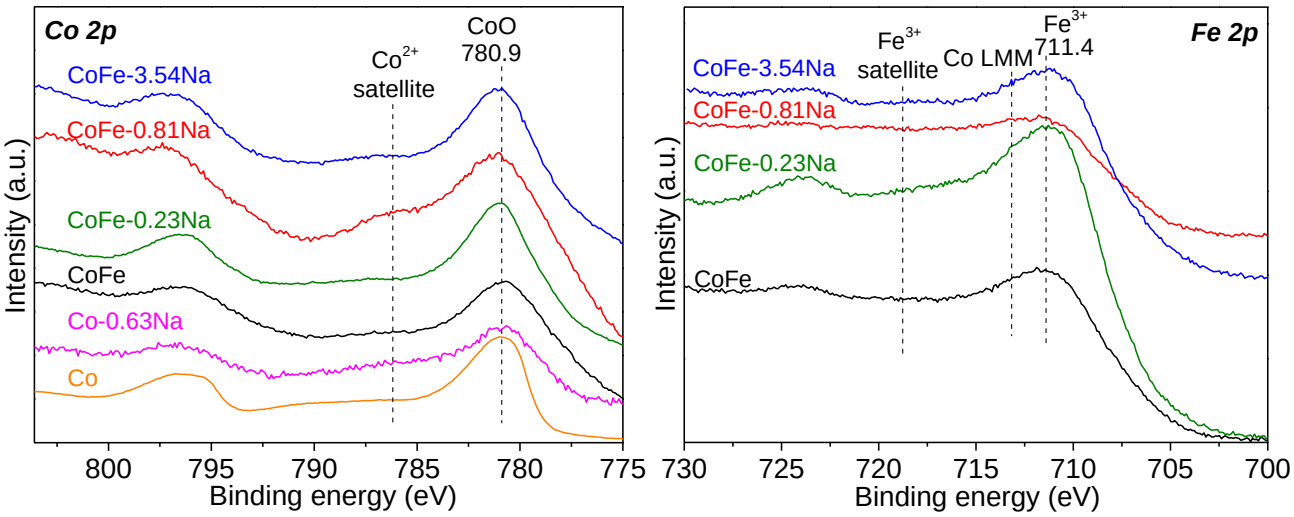

Figure S15. *Ex situ* XPS Co 2p and Fe 2p spectra of the various catalysts after CO_2 hydrogenation reaction for 48 h. The spectra are taken with Al X-ray source.

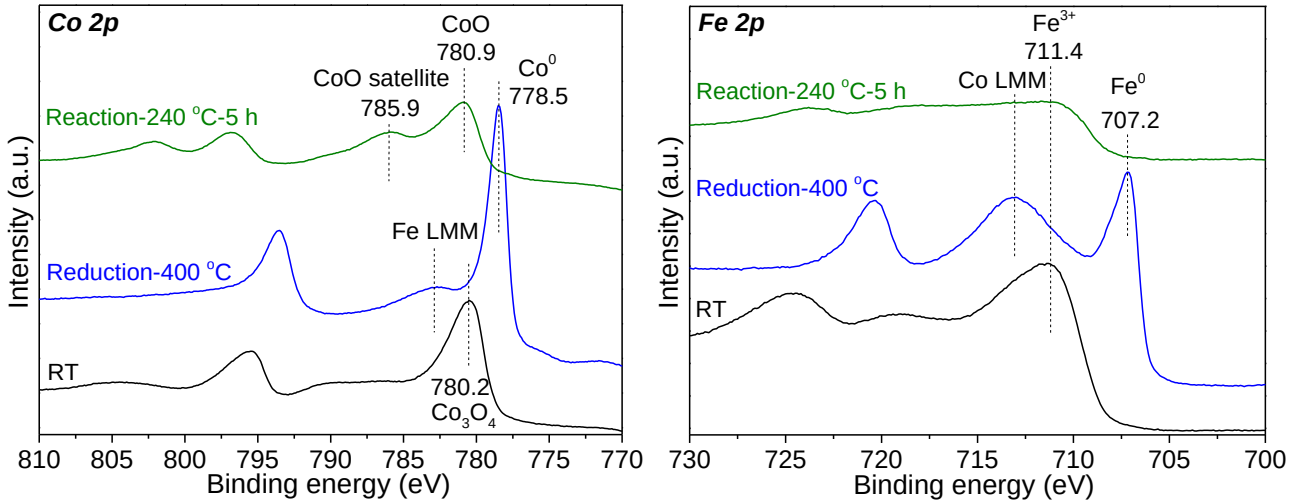

Figure S16. *In situ* XPS Co 2p and Fe 2p spectra of the fresh CoFe-0.81Na catalyst (black curves), after reduction in pure hydrogen (0.1 MPa) at 400 °C for 2 hours (blue curves), after CO_2 hydrogenation reaction at 240 °C (green curves). The spectra are taken with Al X-ray source.

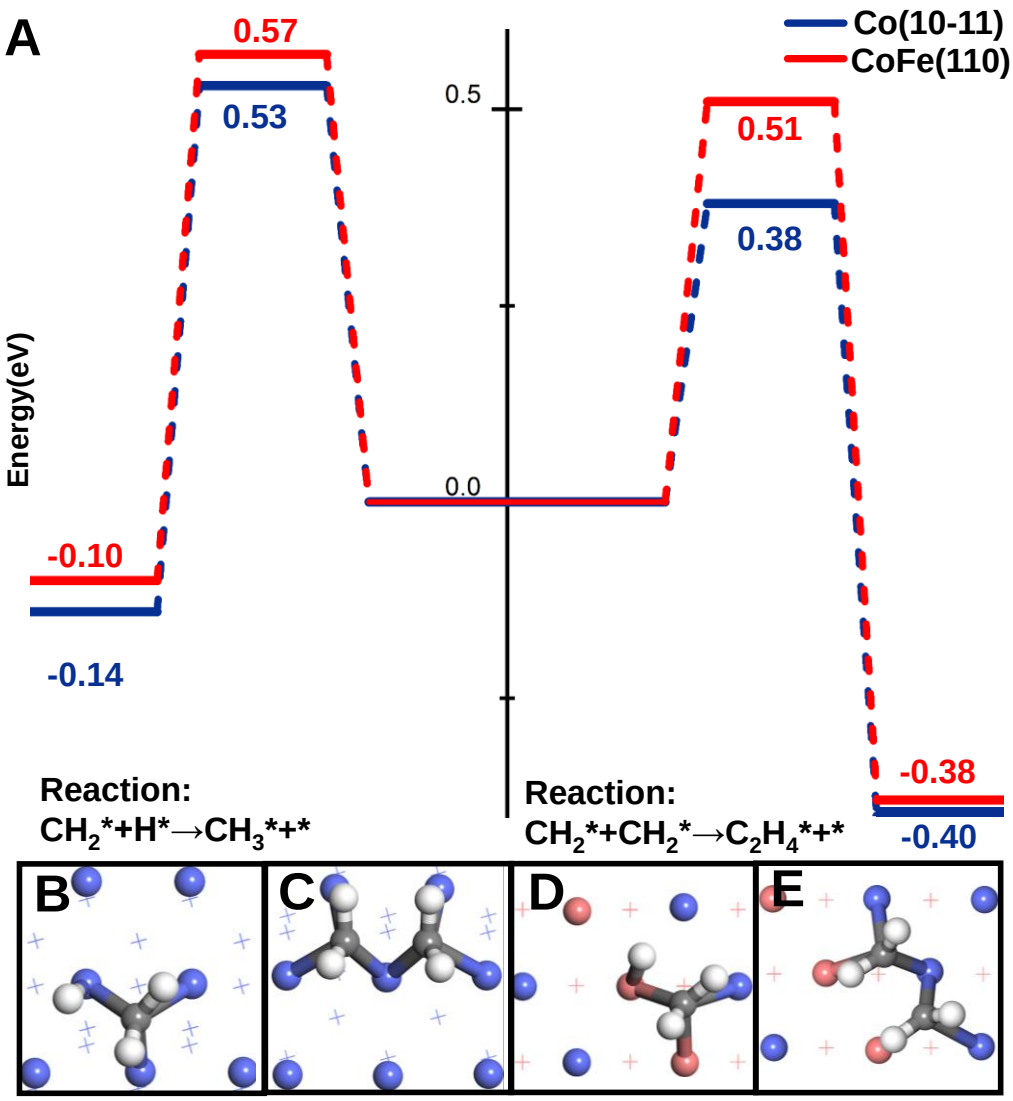

Figure S17. (A) Potential energy profiles for CH_2* hydrogenation vs. self- coupling on the Co and CoFe alloy phases modeled by the Co(10-11) and CoFe(110) slab models. (B–E) Structures of the transition states for CH_2* hydrogenation vs. self- coupling on the above two surfaces, respectively (colors of surface atoms: Co–blue, Fe–magenta, C–grey, H–white).

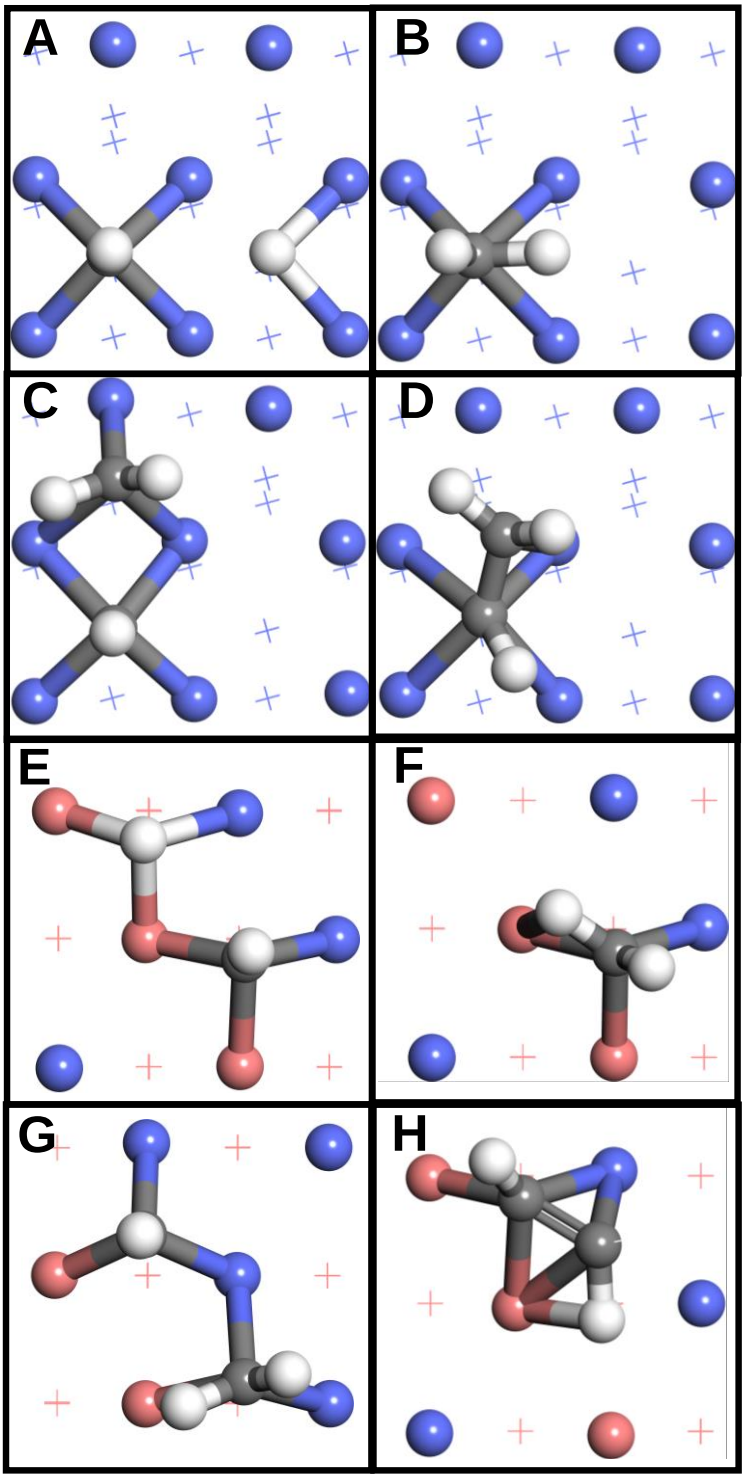

Figure S18. Structures of the initial states and final states for CH* hydrogenation vs. CH*-CH_2* coupling on the (A–D) Co(10-11) and (E–H) CoFe(110) surfaces (colors of surface atoms: Co–blue, Fe–magenta, C–grey, H–white).

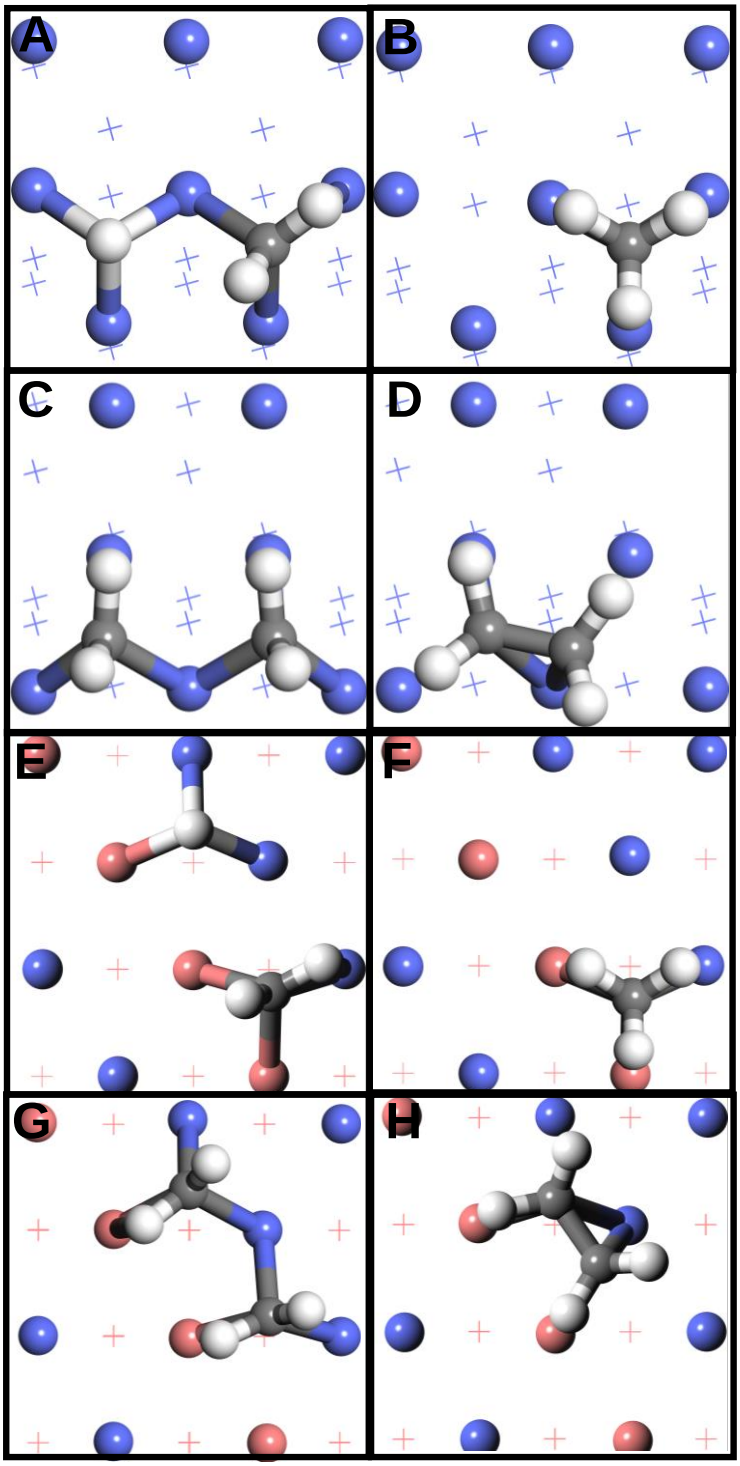

Figure S19. Structures of the initial states and final states for CH_2* hydrogenation vs. CH_2*-CH_2* coupling on the (A–D) Co(10-11) and (E–H) CoFe(110) surfaces (colors of surface atoms: Co–blue, Fe–magenta, C–grey, H–white).

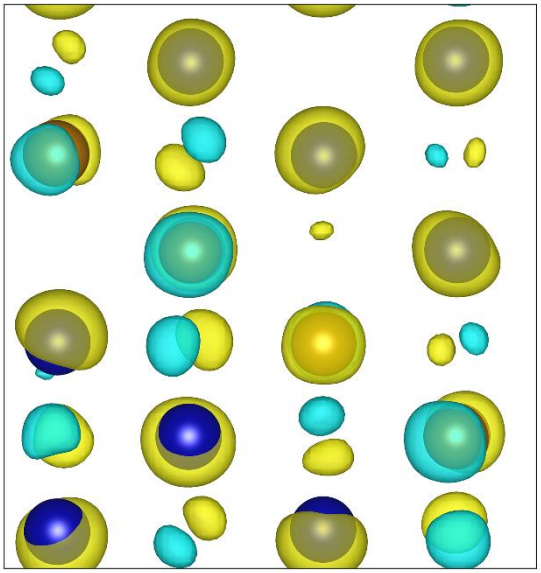

Figure S20. Isosurface of the charge density difference of the Co atoms for the CoFe(110) interface with an isovalue 0.05. Yellow indicates electron accumulation, and light blue indicates electron depletion.

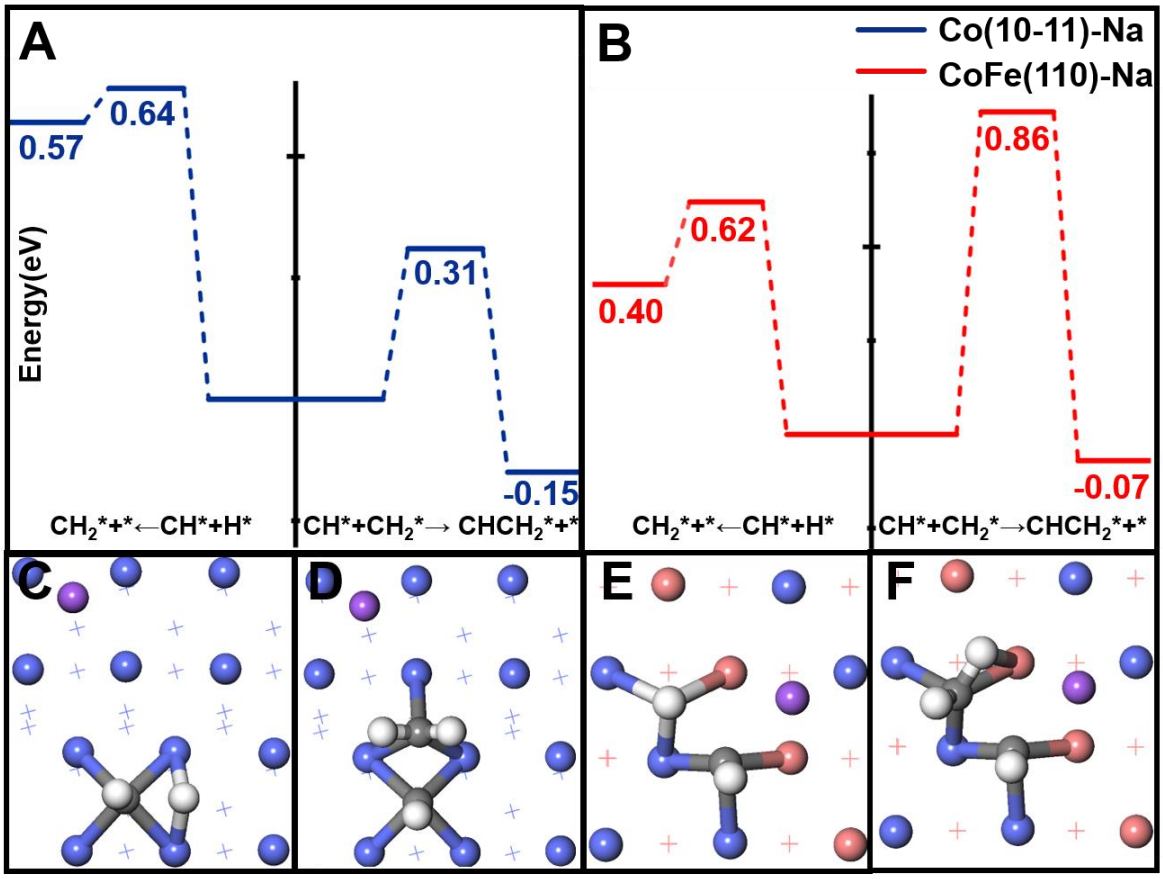

Figure S21. (A and B) Potential energy profiles for CH* hydrogenation vs. CH*+CH_2* coupling on the Na-promoted Co and CoFe alloy phases modeled by the (A) Na/Co(10-11) and (B) Na/CoFe(110) slabs. C–F Structures of the optimized transition states for (C and E) CH* hydrogenation and (D and F) CH*+CH_2* coupling on the (C and D) Na/Co(10-11) and (E and F) Na/CoFe(110) slabs, respectively (colors of surface atoms: Co–blue, Fe–magenta, Na–purple, C–grey, H–white).

Adding the Na promoter to the Co(10-11) surface leads to very similar energy barriers for CH* and CH_2* hydrogenation but a much higher barrier of 0.31 eV for CH*+CH_2* coupling by 0.14 eV and a similar estimated barrier of 0.25 eV for the self-coupling. In addition, all these reactions become thermodynamically less favorable by up to 0.1 eV. When the Na promoter is added to the CoFe(110) surface, the energy barriers of CH* and CH_2* hydrogenation and coupling all increase by 0.1 to 0.25 eV (Figure S21 and Table S6), again consistent with the observed lower CO_2 reactivity and higher CO selectivity using the Na-promoted CoFe alloy catalyst. However, the reaction energies for CH* and CH_2* hydrogenation become more endothermic by 0.15 to 0.25 eV, whereas those for their coupling are more exothermic by up to 0.16 eV.

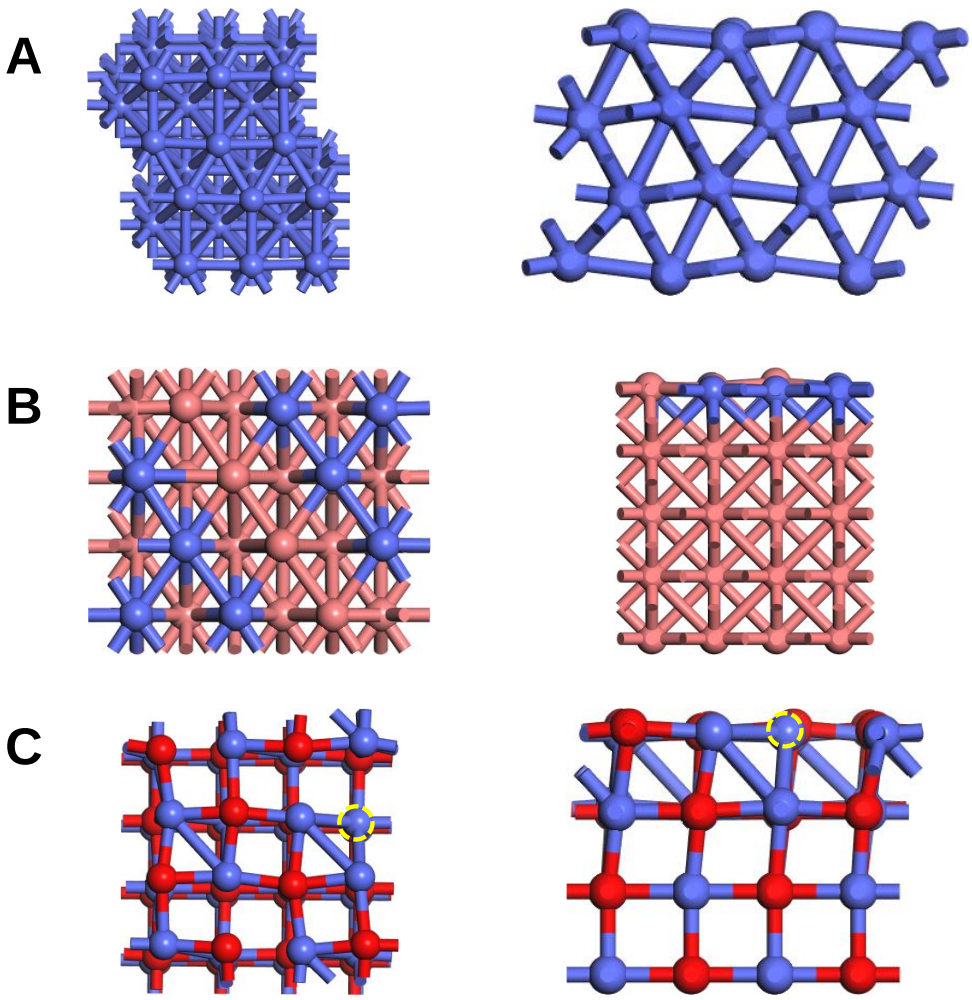

Figure S22. Top (left) and side (right) views of the (A) Co(10-11), (B) Co/Fe(110) and (C) CoO(100) models (additional surface atomic color: O–red). Co is assumed to be in the most stable hcp phase. The CoFe alloy is modeled by partially replacing surface Fe atoms on the most stable Fe(110) slab of the bcc phase. CoO is modeled by its non-polar (100) slab with a surface oxygen vacancy (the yellow circle).

We modeled the Co phase using the Co(10-11) slab surface, as Co exists in the more stable hcp phase. For the CoFe alloy, our experiment suggests it to be in the bcc phase, so we modeled it with the Co/Fe(110) slab surface, as the (110) surface is the most stable one for this phase. For the CoO phase, previous studies suggest that CH_3O dissociation is more favorable at a surface oxygen vacancy site, so we modeled it with the CoO(100) surface with a surface O vacancy. Additionally, CoO was treated as an antiferromagnetic system with a much denser k-point grids for the Brillouin zone.

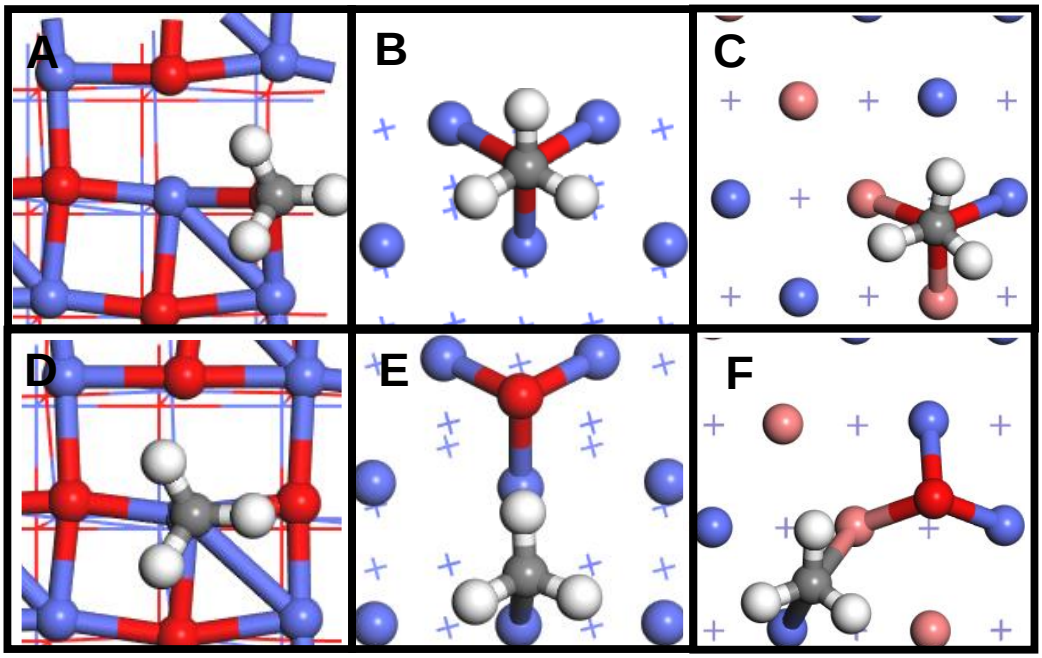

Figure S23. (A–C) Structure of the CH_3O* adsorbate on the (A) CoO(100), (B) Co(10-11) and (C) Co/Fe(110) surface models show in Figure 7. (D–F) The structure after its dissociation into CH_3* and O* on these surfaces.

Supplemental References

1. Nie, X., Meng, L., Wang, H., et al. (2018). DFT insight into the effect of potassium on the adsorption, activation and dissociation of CO_2 over Fe-based catalysts. Phys. Chem. Chem. Phys. ***20***, 14694–14707.
2. Choi, Y.H., Jang, Y.J., Park, H., et al. (2017). Carbon dioxide Fischer-Tropsch synthesis: A new path to carbon-neutral fuels. Appl. Catal., B ***202***, 605-610.
3. Choi, Y.H., Ra, E.C., Kim, E.H., et al. (2017). Sodium-containing spinel zinc ferrite as a catalyst precursor for the selective synthesis of liquid hydrocarbon fuels. ChemSusChem ***10***, 4764-4770.
4. Hwang, S.-M., Han, S.J., Park, H.-G., et al. (2021). Atomically alloyed Fe–Co catalyst derived from a N-coordinated Co single-atom structure for CO_2 hydrogenation. ACS Catal. ***11***, 2267-2278.
5. Yao, B., Xiao, T., Makgae, O.A., et al. (2020). Transforming carbon dioxide into jet fuel using an organic combustion-synthesized Fe-Mn-K catalyst. Nat. Commun. ***11***, 6395.
6. Kwak, J.H., Kovarik, L. and Szanyi, J. (2013). CO_2 reduction on supported Ru/Al_2O_3 catalysts: Cluster size dependence of product selectivity. ACS Catal. ***3***, 2449–2455.
7. Li, S.W., Xu, Y., Chen, Y.F., et al. (2017). Tuning the selectivity of catalytic carbon dioxide hydrogenation over iridium/cerium oxide catalysts with a strong metal-support interaction. Angew. Chem., Int. Ed. ***56***, 10761–10765.
8. Chen, X., Peng, M., Cai, X., et al. (2021). Regulating coordination number in atomically dispersed Pt species on defect-rich graphene for n-butane dehydrogenation reaction. Nat. Commun. ***12***, 2664.
9. Peng, M., Dong, C.Y., Gao, R., et al. (2021). Fully exposed cluster catalyst (FECC): Toward rich surface sites and full atom utilization efficiency. ACS Cent. Sci. *7*, 262–273.
10. Ashworth, D.J., Roseveare, T.M., Schneemann, A., et al. (2019). Increasing alkyl chain length in a series of layered metal-organic frameworks aids ultrasonic exfoliation to form nanosheets. Inorg. Chem. ***58***, 10837–10845.